Relativistic O VIII Emission and Ionized Outflow in NGC 4051 Measured with XMM-Newton

P. M. Ogle[1], K. O. Mason[2], M. J. Page[2], N. J. Salvi[2], F. A. Cordova[3], I. M. McHardy[4], & W. C. Priedhorsky[5]

[1] *Jet Propulsion Laboratory, California Institute of Technology, MS 238-332, 4800 Oak Grove Dr., Pasadena, CA 91109*

[2] *MSSL, University College London, Holmbury St. Mary, Dorking, Surrey, RH5 6NT, UK*

[3] *4148 Hinderaker Hall, University of California, Riverside, CA 92521*

[4] *University of Southampton, University Road, Southampton, UK*

[5] *Los Alamos National Laboratory, Los Alamos, NM 87545, USA*

pmo@sgra.jpl.nasa.gov

ABSTRACT

We present *XMM-Newton* RGS observations of the soft X-ray spectrum of NGC 4051, and explore their implications for the inner accretion disk and ionized outflow in the active galactic nucleus. We fit the soft X-ray excess with a relativistically broadened O VIII recombination spectrum, including the entire line series and recombination continuum. This plus an underlying power law continuum provides a much better fit to the soft X-ray spectrum than a single temperature or disk blackbody plus power law. The emission line profiles, computed for a Kerr metric around a maximally rotating black hole, reveal a sharply peaked disk emissivity law and inner radius smaller than $1.7R_G$. The spectrum also includes narrow absorption and emission lines from C, N, O, Ne, and Fe in an ionized outflow. Outflow column densities are relatively low and do not create significant edges in the spectrum. The small amount of absorption bolsters confidence in the detection of relativistic emission line features. The narrow-line emitter has a large (76%) global covering fraction, leading to strong forbidden lines and filling in of the resonance absorption lines. We also find broad C VI Lyα and very broad O VII emission from the broad-line region. The narrow and broad-line regions span large ranges in ionization parameter, and may arise in a disk outflow. The ionized absorber has a large ionization range which is inconsistent with pressure equilibrium in a multiphase medium. The mass outflow rate exceeds the accretion rate by a factor of one thousand.

Subject headings: galaxies: active—Xrays: galaxies — galaxies: individual (NGC 4051)

1. Introduction

Study of relativistic emission lines in the X-ray spectra of Seyfert galaxies has the potential to elucidate the nature of the accretion disk and spacetime geometry near supermassive black holes. A very broad feature was observed by *ASCA* near the energy of the 6.4 keV Fe Kα line in MCG-6-30-15 (Tanaka et al. 1995) and other Seyfert galaxies (Nandra et al 1997b). Convincing examples measured by *XMM-Newton* include MCG-6-30-15 (Wilms et al. 2001) and Mrk 766 (Page et al 2001; Mason et al. 2003). The current best explanation for this feature is Doppler and gravitationally broadened Fe K-shell emission from an accretion disk which extends close to the innermost circular orbit of a supermassive black hole (Fabian et al. 1989).

The recent discovery of relativistic emission lines in the *soft* X-ray spectra of MCG-6-30-15 and Mrk 766 (Branduardi-Raymont et al. 2001) may help to reveal the ionization structure and elemental abundances in the accretion disk. The O VIII, N VII, and C VI Lyα emission lines probe high ionization states which may arise in the photoionized surface of the disk. This is complementary to studies which have indicated emission from highly ionized Fe in these same galaxies (Wilms et al. 2001; Mason et al. 2003).

Ionized accretion disk models have been compared to the observations, but have yet to be explicitly fit to grating spectra. The predicted emission line equivalent widths depend primarily on the vertical ionization structure and abundances in the top layer of the accretion disk. Both constant density (Ballantyne, Ross, & Fabian 2002) and hydrostatic balance (Nayakshin, Kazanas, & Kallman 2000) have been used to set the density profile of the disk. Together with the disk illumination law, this determines the ionization structure. Constant density slab models predict O VIII Lyα equivalent widths of 30-70 eV for a disk with solar abundances (Ballantyne, Ross, & Fabian 2002). The observed O VIII equivalent widths in MCG-6-30-15 and Mrk 766 are 2-5 times these predicted values. However, the optical depth of the photoionized skin can be increased by raising the ratio of disk flux to X-ray flux, explaining the observed O VIII Lyα equivalent widths (Sako et al. 2003a).

More problematic are the very strong N VII Lyα emission lines and lack of Fe L-shell lines observed in MCG-6-30-15 and Mrk 766. The observed equivalent widths require N/O abundance ratios which are several times solar. Radiative transfer effects may be important for explaining the anomalous emission line ratios. It is possible to pump the N VII Lyα

emission line with O VIII Lyα photons via Bowen resonance fluorescence Sako (2003b). The lack of relativistic Fe L-shell lines may be explained by a large O VIII edge opacity, while the O VIII Lyβ line could be suppressed by resonance scattering (Sako et al. 2003a). It is also essential to model the effects of an overlying ionized absorber component (Mason et al. 2003).

An alternative model has been proposed to explain the soft X-ray spectral features in MCG-6-30-15 and Mrk 766 by absorption edges from neutral Fe in dust instead of relativistic emission lines (Lee et al. 2001). The apparently reddened optical-UV continuum, strong X-ray absorption, and weak UV/X-ray flux ratio in MCG-6-30-15 (Reynolds et al. 1997a) supports the notion of a dusty ionized absorber. In this model, the dust must be embedded in a highly ionized medium in order to avoid strong edges from neutral He, C, and N which would obliterate the X-ray spectrum at the column densities inferred from the optical reddening. However, Mason et al. (2003) and Sako et al. (2003a) argue against the dusty ionized absorber model based on the lack of strong Fe I resonance absorption features which should attend the putative Fe L-shell edges. The lack of intrinsic O I K-edges in the *XMM-Newton* RGS spectra of MCG-6-30-15 and Mrk 766 is further evidence against silicate dust.

Low resolution observations of NGC 4051 with EXOSAT (McHardy et al. 1995) and ASCA (Guainazzi et al. 1996) indicated the presence of variable absorption features at 0.6-0.9 keV. These were interpreted as O VII and OVIII edges from an ionized absorber along the line of sight to the X-ray continuum source. Grating observations of NGC 4051 and several other sources reveal a more complicated picture. Resonance absorption lines and unresolved transition arrays (UTAs) are responsible for much of the soft X-ray spectral complexity in Seyfert galaxies. In hindsight, it is obvious that resonance absorption lines can be much stronger and appear at much lower column densities than photoionization edges. High resolution *Chandra* and *HST* grating spectra of the ionized X-ray and UV absorbers in NGC 4051 are reported by Collinge et al. (2001). There are multiple blue-shifted absorber components, and re-emission is seen from narrow X-ray lines.

NGC 4051 is classified as a narrow-line Seyfert 1 galaxy (NLS1). In order to avoid confusion when talking about the different emission line regions, we refer to them as follows. The narrow-line region (NLR) has the lowest velocity and turbulent velocity (FWHM< 5×10^2 km s^{-1}). The broad-line region (BLR) has larger velocity width ($5 \times 10^2 - 3 \times 10^4$ km s^{-1}). The relativistic-line region (RLR) has the largest velocity width ($> 3 \times 10^4$ km s^{-1}) and is also affected by gravitational redshift. Note that this classification is based purely on velocity, which increases closer to the central black hole. We avoid a classification based on density, for as we shall show, both the NLR and BLR (and perhaps RLR) encompass a large

range of ionization parameter and density.

In this paper, we present the *XMM-Newton* RGS spectrum of NGC 4051 (z = 0.00234). Our long (122 ks) observation reveals unprecedented detail in the soft X-ray spectrum. We interpret a very broad spectral feature as relativistic O VIII emission from the inner accretion flow around the central black hole. We also fit models of the ionized absorber and emitter spectrum, including inner-shell absorption from a number of ions.

2. Observations

We observed NGC 4051 for a full orbit with *XMM-Newton* on 16-17 May 2001. The OM and EPIC light curves are reported by Mason et al. (2002) and the EPIC spectral variability is analyzed by Salvi (2003) and Salvi et al. (2003b). The X-ray flux varied significantly during the observation with a period of particularly low flux approximately half way through (Mason et al. 2002). During the last 14 ks of the observation the particle background increased dramatically. We have excluded these data from the analysis. The spectrum during the 8.4 ks period of lowest flux ("low state", 0.3-2.0 keV EPIC PN+MOS count rate < 8 count s^{-1}) was reduced separately from the remaining 99 ks ("high state") of the observation.

The RGS spectrum (Fig. 1) was reduced using the *XMM-Newton* SAS v5.2. The response matrices were corrected for imperfections in the effective area calibration using the data/model ratios from a power law fit to the RGS spectra of Mrk 421. After this correction the individual first and second order spectra from RGS1 and RGS2 were added together and the response matrices were combined accordingly. The absolute effective area of RGS is calibrated to better than 5% (den Herder et al. 2001).

The spectral resolution of RGS in first order is FWHM= 72 mÅ, and the wavelength calibration is accurate to 8 mÅ (den Herder et al. 2001). These correspond to FWHM= 620 km s^{-1} and $\Delta v = 69$ km s^{-1} at 35 Å. The spectral bins range from 20-40 mÅ in width from the low to high wavelength ends of the spectra, so we oversample by a factor of 2-4. The high-state spectrum has 50-570 photons/bin, while the low-state spectrum has 2-22 photons/bin. There are enough photons/bin in the high-state spectrum to use $\sqrt{N}$ Poisson errorbars and fit our models using the χ^2 statistic. For the low state, we use the C-statistic (Cash 1979) and plot asymmetric Poisson errorbars (Gehrels 1986).

The combined *XMM-Newton* EPIC, RGS and Optical Monitor (OM) measurements (Salvi 2003) constrain the photoionizing portion of the NGC 4051 spectral energy distribution (SED, Fig. 2). The UV flux points at 2100, 2300, and 2900 Å were computed from the

mean count rates in the UVW2, UVM2, and UVW1 bandpasses and corrected for Galactic reddening (Salvi 2003; Mason et al. 2002). Additional radio, IR, and optical flux points were obtained from the NASA Extragalactic Database (NED). The soft X-ray slope of $\Gamma = 2.4$ is from our best fit model to the high-state RGS data. The hard X-ray slope of $\Gamma = 1.5$ is from the best fit PL to the high-state EPIC PN data. We assume that the SED has a high-energy cutoff above 100 keV. Integrating over the SED, the bolometric luminosity is $L_{\rm bol} = 2.7 \times 10^{43}$ erg s^{-1} and the ionizing (13.6 eV-13.6 keV) luminosity is $L_{\rm ion} = 4.1 \times 10^{42}$ erg s^{-1} during the high-state.

We retrieved archival *Chandra* HETGS observations taken during 2000 April 24-25 for comparison with the 2001 May *XMM-Newton* data set. The Medium Energy Grating (MEG) data are most useful for assessing the nature of the soft X-ray excess, and have been analyzed in detail by Collinge et al. (2001). We reprocessed the MEG $\pm 1^{st}$ order spectra from the Level 1 event file using CIAO 3.0.1 and the associated CALDB 2.23 calibration database. We combined events from the entire 82 ks of the observation to get the mean spectrum. The two first order spectra were added and the resultant spectrum was rebinned to 0.05 Å to improve the statistics at long-wavelengths. This yielded 10-270 counts per bin, enabling us to use Poisson errorbars and to use χ^2 as a fit statistic. The unbinned MEG spectra are too noisy to allow a meaningful analysis at the full 0.023 Å resolution of the spectrograph.

3. Spectral Models

3.1. Continuum

The high state RGS spectrum of NGC 4051 is far from a simple power law (Fig. 1). There is a large soft X-ray excess over the underlying soft power law, apparent as a broad bump from 13-32 Å. The spectrum is punctuated by many narrow absorption lines, but there are no deep absorption edges. There are several narrow emission lines which contribute a small percentage of the soft excess seen in the lower resolution EPIC spectrum (Salvi et al. 2003b). The nature of the curvature in the soft spectrum is not obvious, and has previously been ascribed to blackbody emission (Guainazzi et al. 1996; Collinge et al. 2001).

We use the IMP[1] (v1.1) spectral fitting code developed at UCSB (Brookings & Ogle 2003; Ogle & Brookings 2003) to fit the high-state RGS spectrum. All fits include Galactic absorption with column density $N_{\rm H} = 1.32 \times 10^{20}$ cm^{-2} (Dickey & Lockman 1990). They also include narrow absorption and emission from the intrinsic ionized outflow, which we

---

[1]IMP and its documentation are available at http://xmmom.physics.ucsb.edu/~pmo/imp.html

discuss in detail below. We adopt a distance of 9.35 Mpc, derived from the host galaxy kinematic redshift assuming $H_0 = 75$ km s^{-1} Mpc^{-1}, to convert from flux to luminosity. Unless otherwise stated, single parameter error estimates are for 90% confidence.

We first try fitting a power law plus single temperature blackbody to the RGS spectrum (Fig. 1a). This model gives a formally poor fit ($\chi^2/DF = 1.56$). The blackbody peak is broader than the observed soft excess. This is compensated by a deep O VII edge at 17 Å which appears to be overestimated by the model. The best fit temperature for the blackbody is $kT = 0.14$ keV, and the underlying power law has photon index $\Gamma = 2.2$. These are similar to the results of Collinge et al. (2001), who suggest that residuals to their blackbody fit represent additional spectral complexity from absorption.

A power law plus multicolor disk blackbody gives a worse fit ($\chi^2/DF = 1.66$). The best-fit black hole mass for this model is $5 \times 10^3 M_\odot$. The inner radius of the accretion disk is $1.3 R_G$, and the accretion rate is 60% of the Eddington rate. While the model roughly fits the shape of the soft X-ray continuum, it underpredicts the UV flux and bolometric luminosity by a large amount (Fig. 2). It is inconsistent with reverberation studies which yield a much larger black hole mass of $\sim 10^6 M_\odot$ (Peterson et al. 2000; Shemmer et al. 2003). For such a large central mass, a disk blackbody should peak in the far-UV, not the X-ray band.

It is unlikely that the soft excess is the Wien tail of a Comptonized blackbody. We tested this possibility with the IMP *comptt* model (Titarchuk 1994). The observed spectral slope isn't nearly steep enough, especially at the long wavelength end of the RGS spectrum. The shape of such a model is so far off, that we do not attempt to fit it to the data. A Wien tail absorbed by neutral carbon in a dusty ionized absorber appears to be ruled out since there is no other indication of dust absorption in the spectrum of NGC 4051.

For the sake of completeness, we also try a power law plus optically thin bremsstrahlung model (Fig. 1b). This gives a worse fit than the blackbody model ($\chi^2/DF = 1.69$). The best fit plasma temperature is $kT = 0.83$ keV, and the emission measure is 9.8×10^{64} cm^{-3}. Because the roll-over in the bremsstrahlung spectrum is not steep enough to match the observed spectral bump, the model compensates by overestimating the O VII edge depth.

Conventional continuum emission processes can not explain the observed spectral bump, so we turn to discrete atomic processes. Unlike MCG-6-30-15 (Lee et al. 2001), the spectral break at 17 Å is much too broad to be explained by O VII K and Fe I L photoionization edges from the ionized absorber. As we show below, the observed column densities of O VII and Fe I in the ionized absorber are too small to give appreciable edges.

3.2. Relativistic Lines

Next we model the soft X-ray spectrum with a power law plus relativistic O VIII Lyα emission line. We assume line profiles from an accretion disk which may extend to the inner stable circular orbit of a maximally rotating Kerr black hole (Laor 1991). The disk emissivity as a function of radius is assumed to follow a power law R^{-q}. The inner radius is allowed to vary, and the outer radius is fixed at $R_{\mathrm{o}} = 400R_{\mathrm{G}}$, where $R_{\mathrm{G}} = GM/c^2$. This model (REL1, $\chi^2/DF = 1.48$) does better than the blackbody model, but underestimates the flux in the 13-17 Å band (Fig. 3d, e). The extent of the red wing of the line is parameterized by an inner radius of $R_{\mathrm{i}} < 1.5R_{\mathrm{G}}$, and a radial emissivity law with power law index of $q_1 = 5.39$. The disk inclination is $i_1 = 52.7°$.

Our best model (REL2) of the spectrum (Fig. 3a, b, c) includes relativistic emission from the entire O VIII emission line series and radiative recombination continuum (RRC). The line and RRC strengths are computed using the *ionemit* model, which is described in §3.3. We assume that the O VIII ion is photoionized, with an electron temperature of $T_{\mathrm{e}} = 2 \times 10^6$ K (consistent with $\log \xi = 3.4$, see §4.2). For simplicity, we assume that all emitted line photons escape directly and do not treat their radiative transfer. Radiative transfer effects could alter the observed line ratios. For example, Lyβ photons may be down-converted to Lyα if the emission region is optically thick.

The REL2 model has $\chi^2/DF = 1193/901 = 1.32$, a significant improvement over REL1 ($\Delta\chi^2 = 201$ for one additional degree of freedom). The combined Lyβ plus higher order lines account for the gradual steepening of the spectrum in the 13-17 Å band. We map cross-sections of the χ^2 surface in (R_{i}, q, i, Γ) parameter space (Fig. 4), parameters which have the largest influence on the relativistic line shape. There is a well-localized minimum in each of these plots, demonstrating that we can accurately constrain disk parameters. We adopt the 3σ (99.7%) confidence region for variation in two parameters as a conservative bound on these parameters, given possible systematic uncertainties in the underlying continuum shape and ionized absorber-emitter models.

The breadth of the relativistic O VIII line profiles is parameterized by an inner disk radius of $R_{\mathrm{i}} < 1.7R_{\mathrm{G}}$ at 99.7% confidence (Fig 4a, b, c). As far as we are aware, this is the closest distance to the event horizon of a supermassive black hole ever measured. If the line emission comes from outside the innermost stable circular orbit (ISCO), it implies a black hole spin parameter of $j > 0.973$, approaching the maximal value. Emission from *inside* the ISCO is not excluded, but would require an extension of our model. The greatest uncertainty on the disk inner radius comes from modeling the underlying continuum. Decreasing the power law index by 0.1 dex from the best fit value increases R_{i} from 1.24 to 1.6 R_{G}, and still yields and acceptable fit (Fig. 4c).

There is some degeneracy between the disk emissivity index and the disk inclination (Fig. 4c), since both affect the energy of the blue shoulder of the relativistic line profile. However, the emissivity index is still well constrained to be $q_2 = 5.0^{+0.5}_{-0.2}$, at 99.7% confidence for variation in 2 parameters. This means that nearly all ($> 99\%$) of the O VIII emission comes from within 6 $R_{\rm G}$ and the half-light radius is $1.6R_{\rm G}$ (for $R_i = 1.24R_{\rm G}$). A steep radial emissivity law ($q = 3.5$) is predicted for a black hole accretion disk with non-zero torque at the ISCO (Agol & Krolik 2000). The relativistic lines in Mrk 766 and MCG-6-30-15 (Branduardi-Raymont et al. 2001) have emissivity indices of $q = 3.6 - 3.8$ and half-light radii of $\sim 1.9R_{\rm G}$, which are similar to this prediction. The radial emissivity index for the relativistic O VIII line in NGC 4051 is much steeper, implying that it originates from a narrower range of radii.

The energy of the blue shoulder of the relativistic O VIII Lyα line profile is sensitive to and increases with disk inclination. The best-fit disk inclination for NGC 4051 is $i_2 = 48^{+4\circ}_{-3}$, again at 99.7% confidence for variation in 2 parameters. This value is correlated with q_2, with steeper values of the emissivity index yielding larger disk inclination. We have not included smearing from Compton scattering, which could lead to an overestimate of the energy of the blue shoulder and hence the inclination. It is also possible that a flare or warp to the inner disk or other time dependent structure will affect the inclination. With these caveats in mind, we find that the disk inclination in NGC 4051 is significantly different from the inclinations ($36°$, $40°$) inferred from the relativisitic line profiles in Mrk 766 and MCG-6-30-15 (Branduardi-Raymont et al. 2001). This is to be expected from AGN viewed at different angles. The disk inclination is also consistent with the $48 \pm 5°$ inclination of the conical NLR outflow in NGC 4051, derived from [O III] imaging and spectroscopy (Christopoulou et al. 1997). This alignment is remarkable given the much larger size scale of the NLR and may indicate an intimate connection between the NLR and accretion disk.

The relativistic O VIII Lyα flux is $F = 3.5 \pm 0.1 \times 10^{-3}$ ph s^{-1} cm^{-2} and the equivalent width is 88 ± 3 eV. Using a curve-of-growth analysis, the observed EW requires an O VIII column density of $\sim 10^{19}$ cm^{-2} for a reasonable turbulent width of $b \leq 10^4$ km s^{-1} (Socrates, Davis, & Blaes 2003) and a covering fraction of unity. The O VIII Lyα line is dominated by its damping wings in this region of parameter space. The sum of relativistic O VIII line series equivalent widths is 164 ± 5 eV. The model Lyα to Lyβ flux ratio is 3.8-4.7, and the ratio of RRC to Lyα is 0.19-0.23. The exact ratios depend on the O VIII column density and Doppler parameter in the accretion disk. These are not well constrained by the model fit, owing to severe blending of higher order lines and RRC.

There are no relativistic lines from N VII or C VI in the NGC 4051 spectrum. We put upper limits (at 90% confidence) of 4×10^{-4} and 6×10^{-4} ph s^{-1} cm^{-2} on the Lyα fluxes

of these two ions, assuming all of the relativistic line profiles are the same. The photon flux ratios with respect to O VIII Lyα are then < 0.09 for N VII Lyα and < 0.14 for C VI Lyα. As we discuss in §4.2, these limits are consistent with solar abundances in a highly ionized plasma. In comparison, the ratios observed in Mrk 766 (1.0 and 0.8 , respectively) are more difficult to explain (Mason et al. 2003; Sako 2003b).

The underlying soft power law continuum in the REL2 model has $\Gamma = 2.35$ (for $R_i = 1.24 R_G$) and a normalization of $3.85 \pm 0.02 \times 10^{-4}$ ph s^{-1} cm^{-2} Å^{-1} (at 1 Å). This yields a high-state 0.3-10 keV luminosity of $L_x = 5.9 \times 10^{41}$ erg s^{-1} from the soft power law. We note that other shapes for the soft X-ray continuum are conceivable, and the chosen continuum may have an affect on the relativistic line parameters. However, lacking a physical model for the continuum, a power law is often used and is consistent with the expectation of a Compton-scattered accretion disk spectrum.

We try adding an intrinsic neutral absorber to the REL2 model and find a best fit value of $N_{H,int} = 1.1 \pm 0.4 \times 10^{19}$ cm^{-2} and no significant improvement in the fit. This is consistent with the result of Collinge et al. (2001), who find an upper limit of $N_{H,int} \sim 10^{20}$ cm^{-2} from their *Chandra* HETGS observation.

3.3. Ionized Outflow

The RGS spectrum has strong, narrow K-shell absorption lines from C V-VI, N VI-VII, O VII-VIII, and Ne IX (Fig. 5). We detect weaker L-shell absorption lines from Fe XVII-XX and inner-shell absorption from N IV-V, and O IV-VI. Narrow H-like, He-like, and Fe L-shell lines are also seen in emission. O VII and Ne IX forbidden emission lines are particularly strong, since they are not absorbed. The large equivalent width of O VII f indicates a large global covering fraction for the X-ray NLR, estimated below. We infer that re-emission is important and fills many of the absorption lines, making them appear weaker.

The IMP models *ion* and *ionemit* are used to simultaneously model the ionized absorber and emitter spectra, ion by ion. Absorption lines are modeled by Voigt profiles, with cross-sections from Verner et al. (1996a) and Behar & Netzer (2002). High-order lines are extrapolated using the hydrogenic approximation. Absorption edges are modeled using Verner et al. (1996a) cross sections. The emission line model *ionemit* is described in detail by Ogle et al. (2003). Atomic data are calculated with the Fast Atomic Code (FAC, Gu 2002). We assume optically thin clouds illuminated by a central point source. Level populations are calculated from equilibrium rate equations including terms for photoionization, recombination (RR and DR), photoexcitation, and cascades.

We fit for the line-of-sight covering fractions of both the continuum source and NLR, which we assume are the same for all ions in the absorber. The column densities of the ions in the emitter and absorber are allowed to vary independently. We assume electron temperatures for the emitter in the range $3 - 9 \times 10^4$ K, derived using XSTAR[2] (Kallman & McCray 1982; Kallman 2002) and the observed SED (Fig. 2). The emission is normalized by $f_c L_x$, the product of the covering fraction and 0.3-10 keV luminosity of the soft X-ray power law. We use the best-fit O VII f redshift of $z = 0.0019 \pm 0.0003$ and Doppler parameter of $b = 220 \pm 80$ km s^{-1} for the emitter. The redshift and Doppler parameter of the absorber are fit using all observed lines. We measure velocity with respect to the host galaxy H I kinematic redshift of z=0.00234 (Verheijen & Sancisi 2001).

The mean velocity of the O VII emission region is $v = -130 \pm 90$ km s^{-1}, consistent with the results of Collinge et al. (2001). Allowing for the uncertainty in the RGS wavelength scale, this is consistent with the rest frame of the host galaxy. The best-fit absorber redshift is $z = 0.00100^{+0.00003}_{-0.00007}$, corresponding to a velocity of $v = -402^{+9}_{-20}$ km s^{-1} in the rest frame of the host galaxy. The best-fit absorber Doppler parameter is $b = 212^{+9}_{-6}$ km s^{-1}, which is not directly resolved by RGS. We are able to measure very accurate mean values for the absorber redshift and Doppler parameter by including all of the observed absorption lines in our model fit. However, parameters for the absorber may depend on ionization state. They are also sensitive to redshifts and velocity widths of the resonance emission lines. The mean absorber parameters are consistent with the system observed at $v = -600 \pm 130$ km s^{-1} s^{-1} ($b = 460 \pm 280$ km s^{-1}) with *Chandra* HETGS (Collinge et al. 2001). The outflow speed we measure may be slightly lower because our model takes into account filling in of absorption lines by emission lines.

We do not detect the high velocity system at $v = -2340$ km s^{-1} detected in the co-added HETG spectra of H-like ions (Collinge et al. 2001). It is likely that such a summed absorption spectrum is contaminated by lines from other ions, especially Fe L-shell lines. This procedure is also suspect because Voigt profiles should be added logarithmically, not linearly. RGS does not have as much sensitivity as Chandra to the high ionization lines at short wavelengths, so we can not make a definitive assessment of the presence of the high velocity system in the RGS spectrum. A higher S/N Chandra observation is needed to study individual line profiles.

The best-fit absorber column densities are given in Table 1. They range from 2×10^{15} cm^{-2} for N IV to 4×10^{17} cm^{-2} for O VIII. We calculate peak ionic abundances using the XSTAR photoionization code and observed SED (Fig. 2), and use these to derive equivalent

---

[2]XSTAR documentation is available at http://heasarc.gsfc.nasa.gov/docs/software/lheasoft

hydrogen column densities of 3×10^{19} to 3×10^{21} cm^{-2}. There is a trend of increasing column density with increasing ionization parameter (Fig. 6). The N II ion (below the ionization range plotted in Fig. 6) has an anomalously large column density (Table 1). We expect a smaller column density than N III, which is undetected, so we are suspicious of the N II 1s-2p line identification.

The O VII and O VIII column densities in the absorber correspond to K-edge optical depths of $\tau = 7.3 \times 10^{-2}$ and 3.8×10^{-2}, respectively. As we noted above, these weak edges have little effect on the shape of the continuum spectrum. In comparison, Collinge et al. (2001) find apparent oxygen edge depths of 3-4 times greater in their analysis of the HETG spectra. However, they conclude that these are inconsistent with an absorption line curve-of-growth analysis which indicates smaller column densities. We surmise that their overestimate of edge depths is due to an inaccurate continuum model and neglect of Fe L-shell absorption. The upper limit on the Fe I column density in the RGS spectrum (Table 1) corresponds to $\tau < 3.0 \times 10^{-3}$ at the Fe I L edge, and there is no other indication of silicate or iron oxide dust absorption.

The best fit emitter column densities are given for H-like and He-like ions in Table 1. They lie in the range 4×10^{15} to 3×10^{17} cm^{-2}. Except for C V which is not detected, they are within a factor of 2.6 of the corresponding absorber column density. This is reassuring, and is consistent with the emitter and absorber coming from the same system of NLR clouds. We do not expect them to be identical, since there are likely to be fluctuations in NLR column density. Absorption probes a pencil beam through the NLR while emission is integrated over the entire NLR.

We fit simultaneously for covering fraction as well as column density and Doppler parameter. The best-fit line-of-sight covering fraction of the NLR emitter by the absorber is pegged at $f_{\rm los} = 1.0^{+0}_{-0.02}$, indicating that the bulk of the NLR lies interior to the absorber. This, plus the small difference in redshift between the absorber and emitter accounts for the partial filling in of the resonance absorption lines and the apparent absence of strong 2p-1s (r) resonance emission lines from N VII, O VII, OVIII, and Ne IX. The best-fit line-of-sight covering fraction of the continuum source by the absorber is also > 0.98. This rules out any significant source of extended soft X-ray continuum.

The 0.3-10 keV ionizing luminosity intercepted by the NLR emitter is $f_{\rm c}L_{\rm x} = 4.5 \pm 0.2 \times 10^{41}$ erg s^{-1}. Dividing by the soft power law continuum luminosity gives an estimate of $f_{\rm c} = 0.76 \pm 0.03$ for the NLR global covering fraction. This accounts for the large equivalent widths of the narrow forbidden emission lines. We caution that this covering fraction estimate may be rendered more uncertain by continuum variability and reverberation effects. However, the high-state continuum flux we observe is similar to the 1996-2003

historical average (Uttley et al. 2003a), mitigating these effects.

We treat C VI separately from other ions in our model. The C VI RRC is much stronger than expected, considering the apparently weak C VI 2p-1s (Lyα) emission line. This and the P-Cygni profile show that C VI Lyα is heavily absorbed. The C VI emitter has a larger blueshift than the other ions, corresponding to $v = -310^{+70}_{-20}$ km s^{-1}. The emitter turbulent velocity width is much larger than the other ions ($b = 700 \pm 40$ km s^{-1}, FWHM = 1200 km s^{-1}), putting it in the BLR. The C VI absorber also has a larger turbulent velocity ($b = 410 \pm 20$ km s^{-1}) than other ions, but has the same blueshift. It covers a large fraction of the C VI emitter, with $f_{\mathrm{los}} = 0.88 \pm 0.02$. The narrow emission line component of C VI Lyα may be seen at 33.8 Å as a $\sim 3\sigma$ residual to the fit (Fig. 5). All of this indicates that C VI emission arises primarily in the BLR. Kaastra et al. (2002) find a similar (though much broader) C VI Lyα line in NGC 5548 which they attribute to the BLR.

The C VI RRC is strong enough to fit for the BLR electron temperature which determines its width. We estimate $T_{\mathrm{e}} = 4.0^{+3.3}_{-1.3} \times 10^4$ K, which is consistent with the value 3.2×10^4 K predicted by XSTAR for a photoionized nebula with maximum C VI abundance. The rest of the RRCs are too weak or blended to measure accurately.

In addition to narrow O VII emission, there appears to be broad emission at the location of the O VII 2p-1s (r) line (Fig. 5). Adding a broad Gaussian to the fit improves it by a significant amount ($\Delta\chi^2 = 27$, for 3 additional degrees of freedom). The best-fit parameters are $\lambda = 21.7 \pm 0.1$ Å, $\sigma = 0.33 \pm 0.08$ Å, and a flux of $2.2 \pm 0.7 \times 10^{-4}$ ph s^{-1} cm^{-2}. This indicates a component of O VII emission from the BLR with FWHM= $11,000 \pm 3000$ km s^{-1}. Flux from the intercombination lines may also contribute significantly, depending on the BLR density.

Finally, we note some residual absorption lines in the spectrum (Fig. 5). The line at 16.8 Å may be residual Fe XVII absorption which cuts into the O VII RRC. The line at 30.3 Å is narrower than the instrumental response and appears only in RGS1, so is likely to be an unmarked bad column. There is also an unidentified absorption line at 36.4 Å.

3.4. Low State

The low-state RGS spectrum of NGC 4051 (Fig. 7) contains prominent narrow O VII emission lines on a weak continuum. There may be weak Fe L-shell UTA (unresolved transition array) features which contribute to a broad dip in the spectrum from 15-18 Å. Alternatively, this may be a gap between blended narrow Fe L-shell emission lines. Because of the low flux level and short duration of this particular low state, it is not possible to

characterize and measure the spectral features with any great accuracy. NGC 4051 was more recently observed by XMM during an extended low state as a target of opportunity in 2002 November (Uttley et al. 2003a; Page et al. 2003).

We model the low-state spectrum with a small number of components, minimizing the C-statistic to determine the best fit to the data. Our best-fit model has a steep power law continuum with $\Gamma = 2.60$ and a normalization of $4.49 \pm 0.05 \times 10^{-5}$ ph s^{-1} cm^{-2} Å^{-1} at 1 Å. The corresponding 0.3-10 keV luminosity is $L_{\mathrm{x}} = 1.3 \times 10^{41}$ erg s^{-1}. The soft power law continuum index is a bit steeper in the low state than in the high state.

Unlike the high state, there is no obvious curvature or broad bump in the low-state soft X-ray spectrum. We tried adding the relativistic O VIII emission line series, with all disk parameters fixed to high-state values, except for flux normalization. We find a (90%) upper limit of EW< 150 eV for the entire line series. This limit is only slightly smaller than the EW observed during the high state (164 eV). We can neither confirm nor rule out the presence of relativistic line emission during the low state. The EPIC spectra show a correlation between the relativistic O VIII emission and the flux of the soft X-ray continuum (Salvi et al. 2003b). However, it is difficult for EPIC to constrain the relativistic O VIII line flux during the low state.

We include only the strongest absorption and emission line features in our low-state model. The NLR and continuum covering fractions are fixed at 1.0, to match the high state. We find an O VII absorption column density of $1.6^{+0.8}_{-0.5} \times 10^{17}$ cm^{-2} and a Doppler parameter of $b = 230 \pm 30$ km s^{-1} in the narrow absorber. Both are consistent with the parameters observed during the high state. The weak continuum and low S/N make it difficult to derive accurate column densities for the other K-shell ions. In order to quantify the amount of Fe UTA absorption, we assume equal column densities of Fe I-XVI. The best fit mean column density is $1.3 \pm 0.1 \times 10^{16}$ cm^{-2} in each of these ions. The Fe XVII-XX L-shell transitions are too weak to measure.

Two ions in the NLR emitter with measurable column densities are O VII ($4.0\pm0.4\times10^{17}$ cm^{-2}) and O VIII ($4^{+2}_{-1} \times 10^{16}$ cm^{-2}). The O VII emitter column density appears to be a factor of 1.3 greater during the low state than during the high state. However, this difference may be explained by the poor resolution of the low state data, blending of lines in the O VII triplet, or residual emission from the BLR rather than a true variation. The best-fit 0.3-10 keV normalization for the NLR emitter is $f_{\mathrm{c}}L_{\mathrm{x}} = 4.4 \pm 0.3 \times 10^{41}$ erg s^{-1} cm^{-2}, unchanged from the high state.

The O VII f narrow emission line flux is $8.9 \pm 3.8 \times 10^{-5}$ ph s^{-1} cm^{-2} during the low state, compared to $8.8\pm1.6\times10^{-5}$ ph s^{-1} cm^{-2} during the high state. There is no significant

variability, which is consistent with the expected $r > 0.02$ pc size scale of the NLR (§4.4). Dividing $f_c L_x$ from the narrow emission lines by L_x from the power law continuum gives an unphysical global covering fraction of $f_c = 3.5 \pm 0.2$. This is an indication that the NLR does not respond to short timescale variations in the continuum flux, and that values of f_c derived this way are highly uncertain.

3.5. Comparison to *XMM-Newton* EPIC Data

The full EPIC data set and spectral variability are analyzed in detail by Salvi et al. (2003b), and we do not repeat those results here. However we do test for consistency between the RGS and EPIC PN high-state data sets. The EPIC PN data were filtered to exclude the low state and the period of high background during the last 14 ks. We use IMP to fit the 0.3-10 keV band with a model consisting of hard plus soft power laws, relativistically broadened O VIII and Fe XXV K-shell recombination emission (line series + RRC), and two narrow Gaussians to represent O VII and Fe Kα emission lines. The resulting fit and residuals are shown in Fig. 8. The fit is remarkably good ($\chi^2/DF = 1.39$), considering the low resolution of the EPIC camera at soft energies and crudeness of the model relative to our REL2 fit of the RGS spectrum.

The EPIC data are fit by a hard power law with $\Gamma = 1.52$ and a soft power law with $\Gamma = 3.01$. The soft power law is considerably steeper than we find for the RGS data. This points to a cross-calibration problem[3] between the instruments which has been observed for other sources (Kirsch et al. 2003). Uncertainty in the PN response at low energy may be at fault. The mean 2-10 keV EPIC flux for the entire observation, excluding the background flare, is $F_{2-10} = 2.2 \times 10^{-11}$ erg s^{-1} cm^{-2}, corresponding to a luminosity of $L_{2-10} = 2.3 \times 10^{41}$ erg s^{-1}. This is identical to the mean *RXTE* 2-10 keV flux for the years 1996-2003 (Uttley et al. 2003a), indicating that NGC 4051 was in a typical state.

Narrow Fe Kα has a rest energy of 6.41 ± 0.04 keV, consistent with fluorescence from low charge states Fe I-XVIII. The (90% confidence) upper limit to its width is $\sigma = 0.17$ keV, so it is unresolved by EPIC (FWHM$< 18,000$ km s^{-1}). The ratio of the data to a power law with Galactic absorption shows a broad excess in the 4-7 keV region, which may be identified with relativistic Fe Kα (Salvi et al. 2003b). The best fit Laor model has $R_{in} < 2.1 R_G$ and $i \sim 55°$, roughly consistent with relativistic O VIII in the RGS spectrum. The relativistic Fe Kα line flux is 2.1×10^{-8} ph s^{-1} cm^{-2}. The rest energy is $E = 6.70^{+0.01}_{-0.03}$ keV, indicating that Fe XXV is the dominant ionization stage.

---

[3]Calibration document available at http://xmm.vilspa.esa.es/docs/documents/CAL-TN-0018-2-1.pdf

We find significant emission from relativistic O VIII, seen at ~ 0.6 keV in a plot of the ratio of data to the 2 PL continuum (Fig. 8c). It appears more sharply peaked than in the RGS spectrum because of blending with the O VII narrow line. The best fit Laor model has $R_{in} < 1.6R_G$ and $i = 59 \pm 8°$ (Salvi et al. 2003b).

3.6. Comparison to *Chandra* HETGS Data

As discussed above, the broad bump in the NGC 4051 soft X-ray excess has been noted by previous authors, and typically fit by a single-temperature blackbody. Here we test our new interpretation, that this excess is from relativistically broadened O VIII emission, against the 2000 April *Chandra* HETGS observation. The soft X-ray bump is apparent during this epoch (Fig. 9), and has a similar shape to the bump in the 2001 May *XMM-Newton* RGS data. We fit the 1.7-22.6 Å *Chandra* MEG spectrum with IMP, using χ^2 to assess goodness of fit. The model is similar to REL2, but we add a hard X-ray power law to account for the upturn in the spectrum below 5 Å. We also add Ne X, Mg XI-XII emission and absorption to the model, and remove the lower ionization states C V-VI, N II-VI, and O IV-VI which are either too weak to model or are outside the MEG waveband.

The best fit REL model has $\chi^2/DF = 1.59$. One source of residuals may be the effective area calibration uncertainty at the Ir and Au instrumental edges at 5-6 Å. There appear to be additional residuals in the 8-14 Å region from Fe L-shell absorption and emission lines. There is another interesting residual at the location of the narrow O VIII Lyα line, which appears to be stronger than in the *XMM-Newton* observation.

The underlying continuum is fit by the sum of two power laws, a soft power law with $\Gamma = 2.24$ and a hard power law with $\Gamma = 1.30$. The soft slope is similar to that observed with *XMM-Newton* RGS, while the hard slope is 0.2 dex harder than that observed with EPIC in 2001 May. The normalizations are $A_\lambda = 1.51 \pm 0.03 \times 10^{-4}$ ph s^{-1} cm^{-2} Å^{-1} for the soft power law and $A_\lambda = 6.9 \pm 0.2 \times 10^{-4}$ ph s^{-1} cm^{-2} Å^{-1} for the hard power law, both evaluated at 1 Å. The soft X-ray flux at 12.4 Å (1 keV) is a factor of ~ 2 lower in the *Chandra* MEG spectrum than in the *XMM-Newton* RGS spectrum.

The soft X-ray excess is fit with a relativistically broadened O VIII line series and RRC. We assume emission from a Keplerian disk around a Kerr black hole, producing Laor (1991) line profiles. The inner radius is fixed at $R_i = 1.24R_G$ and the outer radius is fixed at $R_o = 400R_G$. The best-fit disk inclination is $50 \pm 1°$. The best-fit index for the radial power law emissivity profile is $q = 5.9 \pm 0.2$, steeper than for the *XMM-Newton* RGS spectrum. If we take into account the positive correlation between i and q (Fig. 4c), and the lack of

long-wavelength coverage of the MEG, we find that the *Chandra* and *XMM-Newton* results are roughly consistent. A more detailed comparison is hampered by the lower S/N in the MEG data at long wavelengths.

We conclude that a relativistic O VIII emission model gives a good fit to the NGC 4051 spectrum for two separate epochs, viewed with two different X-ray observatories. This argues against instrumental effects as the source of the unusual continuum shape. In addition, a secondary soft X-ray bump from 13-17 Å is clearly visible in both the *Chandra* (Fig. 8) and *XMM-Newton* (Fig. 2) data. This detection of high-order emission from the O VIII line series reinforces our interpretation of relativistic line emission from the photoionized inner disk.

4. Discussion

4.1. Basic AGN Parameters

NGC 4051 becomes the third known Seyfert galaxy with strong soft X-ray relativistic lines (SRLs). As noted by Branduardi-Raymont et al. (2001), these all belong to the class of narrow-line Seyfert 1 (NLS1) galaxies. NLS1's Ton S180 (Turner et al. 2001), Ark 564 (Vaughan et al. 1999), and IRAS 13224-3809 (Boller et al. 2003) also display a broad, curved soft excess which may include relativistic emission lines. In addition, these galaxies show evidence for ionized reflection in the hard X-ray band (Ballantyne, Iwasawa & Fabian 2001; Boller et al. 2003). Weaker (EW~20 eV) SRL features may be present in the spectra of broad-lined Seyfert 1's NGC 5548, NGC 4593, and MCG-2-58-22 (Kaastra et al. 2002; McKernan et al. 2003; Salvi et al. 2003a).

NLS1's share a number of unique properties, including 1) narrow hydrogen Balmer emission lines ($v < 2500$ km s^{-1}) (Goodrich 1989), 2) highly variable X-ray spectrum (Leighly 1999a), and 3) steep soft X-ray spectral index (Boller, Brandt, & Fink 1996). These properties may be explained if NLS1's contain lower mass black holes which accrete at higher fractions of the Eddington accretion rate than other Seyfert 1 galaxies. Note that MCG-6-30-15 is a borderline NLS1, with FWHM(Hβ) = 2500 km s^{-1} (Reynolds et al. 1997a) and moderate ($\Gamma = 1.8$) soft X-ray spectral index. However, it tends to be included in this class due to its highly variable X-ray continuum and inferred black hole mass of $\sim 10^6 M_\odot$ (Nowak & Chiang 2000).

Peterson et al. (2000) obtain a reverberation estimate of the mass of the black hole in NGC 4051 of $M = 1.1^{+0.8}_{-0.5} \times 10^6 M_\odot$, roughly a factor of 10 lower than the mass for broad-lined Seyfert 1s with similar luminosities. A similar estimate by Shemmer et al. (2003)

gives $M = 5^{+6}_{-3} \times 10^5 M_\odot$, assuming isotropic circular orbits for the BLR clouds. We adopt the latter, slightly more accurate value for our subsequent analysis. Reverberation mass estimates are subject to uncertainty in the BLR geometry and kinematics (Krolik 2001). The largest uncertainty comes in the case of a thin disk, where projected velocity width goes as $\sin i$ and the virial mass may be severely underestimated for small inclination. However, if the large RLR inclination of 48° also applies to a disk-like BLR, the virial mass is *reduced* by the factor $1/3 \sin^2 i = 0.6$. This reinforces the interpretation that NGC 4051 and NLS1s in general contain relatively low mass black holes. The high inclination can be used to argue against a pole-on orientation as the cause of the narrow permitted lines from the BLR.

From the black hole mass, we compute the Eddington luminosity $L_E \sim 6 \times 10^{43}$ erg s^{-1}. The observed high-state bolometric luminosity is $\sim 50\%$ of the Eddington value. The accretion rate is $\dot{M} = 4.7 \times 10^{-4} \eta^{-1} M_\odot$ yr^{-1}, where η is the efficiency of the accretion process. Assuming a typical value of $\eta = 0.1$, the mass doubling time is $\tau = \ln(2) M / \dot{M} \sim 7 \times 10^7$ yr. At this rate, the AGN could plausibly have originated from a $10 M_\odot$ black hole near the center of NGC 4051 ~ 1 Gyr ago.

4.2. Relativistic Line Region

With 3 objects in the class of strong SRL emitters, we can begin to compare their properties. MCG-6-30-15 and Mrk 766 have similar disk inclinations, emissivity indices, and relativistic N VII/O VIII emission line ratios (Branduardi-Raymont et al. 2001). NGC 4051 stands out for its much broader lines and absence of relativistic N VII emission. It has a steeper ($\Gamma = 2.4$) soft X-ray continuum, compared to $\Gamma = 1.8, 2.1$ in MCG-6-30-15 and Mrk 766 (Sako et al. 2003a; Mason et al. 2003). Of the three objects, NGC 4051 also has the greatest excess variance in its X-ray light curve on short (10-100 ks) timescales (Nandra et al 1997a). The C VI/O VIII emission line ratio ranges from 0.6 in Mrk 766, to 0.15 in MCG-6-30-15 (Branduardi-Raymont et al. 2001), to < 0.14 in NGC 4051. The lack of relativistic C VI Lyα emission may indicate that the inner disk is more highly ionized in NGC 4051 than in MCG-6-30-15 and Mrk 766. This is consistent with a smaller inner disk radius and stronger, steeper, more highly variable soft X-ray continuum.

The strong SRL emitters are parameterized by steep radial emissivity laws, with most of the emission coming from very close to the central black hole. The rapid X-ray continuum variability in NGC 4051 and Mrk 766 is correlated with the relativistic O VIII line variability (Salvi et al. 2003b; Mason et al. 2003), perhaps indicating that the continuum drives the line. (A similar variability analysis has yet to be performed for MCG-6-30-15.) Bright flares (with amplitude $> 100\%$) in the X-ray continuum occur on a timescale of 3 ks (Mason et al.

2002), yielding an upper limit of 50 light minutes ($600R_{\rm G}$) for the size of the flaring regions.

All strong SRL emitters also have relativistic Fe Kα lines. Some (or all) of this emission may come from Fe XXV and Fe XXVI (Mason et al. 2003; Ballantyne, Vaughan, & Fabian 2003; Salvi et al. 2003b) in a photoionized disk. This is especially important for understanding the broad Fe K line in MCG-6-30-15, where so much effort has gone into understanding this emission in terms of Fe I fluorescence. The problems with $> 100\%$ reflection fraction and iron overabundance may disappear if most of the line emission comes from recombination in an ionized disk (Ballantyne, Vaughan, & Fabian 2003).

To characterize the RLR and other emission line regions, we compute XSTAR (Kallman & McCray 1982; Kallman 2002) photoionization models for an optically thin plasma (using the SED in Fig. 2). The illumination of the NLR and BLR is probably well approximated by an r^{-2} drop in flux with radius r from a central point source. The geometry must be more complicated for the RLR, but the central point source assumption is useful for an order of magnitude ionization estimate. In Figure 10, we plot ionization parameter $\xi = L/n_e r^2$ vs. line FWHM. Line width is converted to radius r assuming isotropic circular Keplerian orbits around a central black hole with mass $5 \times 10^5 M_\odot$. For this mass, the innermost circular orbit around a Kerr black hole is at 3×10^{-8} pc (3 light-seconds). The r-ξ parameter space of the ionization map is populated by the emission lines observed in the X-ray and optical-UV spectra, assuming they are produced in regions of peak emissivity. In this way, we estimate the densities needed to explain the ionization levels observed in the RLR, BLR, and NLR.

The relativistic O VIII emission line profile is produced near the inner edge of the accretion disk at $\sim 1.6R_{\rm G}$ from the black hole. Though the emissivity of O VIII Lyα peaks at $\log \xi = 1.7$, there would be strong C VI and N VII Lyα if the ionization parameter of the RLR were this low. The lack of relativistic recombination emission from C VI gives a lower limit of $\log \xi > 3.4$ (Fig. 11). Fe XXV emission peaks at an ionization parameter of $\log \xi = 3.4$ and may contribute to the relativistic Fe K line. The photon flux ratio of relativistic Fe Kα (measured with EPIC) to O VIII Lyα is 0.06. This is close to the peak ratio of Fe XXV/O VIII Ly$\alpha \sim 0.08$ predicted by our XSTAR photoionization model, assuming solar abundances.

Assuming the mean distance from the X-ray source to the surface of the photoionized disk is $1.6R_{\rm G}$, $\log \xi > 3.4$ implies a density of $n_{\rm e} < 1 \times 10^{17}$ cm^{-3} in the RLR. This is only changed by a factor of order unity if we assume a geometry where the disk intercepts half of the flux from an X-ray emitting corona. This upper limit falls between densities predicted for radiation dominated ($n_e = 10^{13}\alpha^{-1}$ cm^{-3}) and gas-pressure dominated disks ($n_e = 10^{20}\alpha^{-7/10}$ cm^{-3}), where $\alpha \sim 0.1$ provides the scaling between pressure and viscous stresses in the disk (Shakura & Sunyaev 1973). However, these are only rough estimates, and do not take into account general relativistic effects on the disk structure around a Kerr

hole (Novikov & Thorne 1973).

N VII and O VIII should coexist at very similar ionization parameters and densities in the inner disk. However, for solar abundances, the nitrogen to oxygen ratio is 0.13, explaining the lack of relativistic N VII emission in the spectrum of NGC 4051. It is actually more puzzling that there is strong relativistic N VII emission in MCG-6-30-15 and Mrk 766 (Branduardi-Raymont et al. 2001), which requires nitrogen overabundances of 6-9 times solar. Alternatively, N VII emission could be pumped by O VIII Lyα via the Bowen resonance-fluorescence mechanism (Sako 2003b). If this is the case, it may indicate a larger N VII optical depth in these two sources than in NGC 4051.

Assuming $\log \xi = 3.4$ in the inner disk, the fraction of oxygen in O VIII is 5.1×10^{-3}. (The rest is in O IX.) The O VIII edge has an optical depth of $\tau \sim 1.0$ for the O VIII column density of $\sim 10^{19}$ cm^{-2} inferred from the relativistic O VIII Lyα EW. For a density of $n_{\mathrm{e}} = 1 \times 10^{17}$ cm^{-3}, this is reached in a thickness of 230 km. For solar oxygen abundance, the Thomson optical depth is 1.5, indicating that electron scattering is the dominant source of opacity in the O VIII Lyα emitting layer. Compton scattering is likely to cause additional line broadening (Ballantyne, Ross, & Fabian 2002), which has not been accounted for in our model. The 2×10^6 K temperature of a layer at $\log \xi = 3.4$ is considerably cooler than the Compton temperature ($\sim 1 \times 10^7$ K).

At the high temperatures and densities inferred for the RLR, there may be a non-negligible contribution from bremsstrahlung to the observed soft X-ray continuum. For $T_{\mathrm{e}} = 2.0 \times 10^6$ K, a bremsstrahlung spectrum cuts off above 0.17 keV, but the exponential tail is potentially observable at the long wavelength end of the RGS band. The emission measure of the relativistic O VIII emission region is $n_{\mathrm{e}}^2 V = 8.2 \times 10^{64}$ cm^{-3} from our REL2 model. Assuming solar abundances and $\log \xi = 3.4$, bremsstrahlung from the RLR could contribute as much as 18% of the total flux at 38 Å. We see no evidence of this in the RGS spectrum, but it can not be excluded. Coverage at longer wavelengths would be useful to put better constraints on this component of the continuum emission.

The detection of higher-order relativistic O VIII emission in NGC 4051 indicates moderate optical depth in the photoionized layer of the accretion disk. It also begs the question of whether or not these lines are present in MCG-6-30-15 and Mrk 766. The sharper line profiles in the latter two objects would lend themselves to detection of the O VIII Lyβ line. However, this region of their spectra is also highly absorbed by Fe UTA features. The absence of Fe UTAs in the high-state spectrum of NGC 4051 yields a simpler model and easier detection. Branduardi-Raymont et al. (2001) identify a sharp feature at 15-16 Å in MCG-6-30-15 which could be O VIII Lyβ from the RLR. However, they argue instead that it may be an O VIII absorption edge. This issue should be revisited in light of our current results, and may

have important implications for the optical depth of the O VIII RLR in these sources.

By extension, we predict emission in Lyβ and higher order lines from relativistic Fe XXV and Fe XXVI in the ionized accretion disk. It will be important to test this hypothesis against higher resolution data from *Astro-E* and *Constellation-X*. This effect may help to distinguish between fluorescence and recombination models of the Fe Kα emission line in Seyfert galaxies. As we find for the O VIII series, including higher order lines in the spectral model may significantly change the accretion disk fit parameters. It will also be important to consider this emission when studying absorption features in the Fe K-shell region (Pounds et al. 2003, e.g.).

We would like to stress that while emission from a Keplerian disk inside a Kerr space-time geometry is consistent with the observed O VIII profile, it is not the only explanation. Alternatively, this emission may come from inside the innermost stable circular orbit of a Schwarzschild black hole (Reynolds & Begelman 1997b). Also, the parameterization of the radial emissivity by a power law is not necessarily correct. Other emissivity laws which peak sharply inside of $1.6R_{\rm G}$ could produce a similar line profile. However, it is unlikely that the observed line profile comes from a two-sided collimated jet or a relativistic wind (Fabian et al. 1995).

4.3. Broad Line Region

The broad C VI Lyα emission line can be produced in the BLR of NGC 4051 at a velocity of 1200 km s^{-1} with $n_{\rm e} = 1 \times 10^{10}$ cm^{-3} at roughly 2×10^{-3} pc (2 light-days) from the central source (Fig. 10). The core of the C IV broad line is produced optimally at a density of $n_{\rm e} = 2 \times 10^{11}$ cm^{-3}. The much lower ionization Hβ line has a similar velocity width (FWHM= 1100 km s^{-1}) and reverberation size of 3 ± 1.5 light days (Peterson et al. 2000; Shemmer et al. 2003), and would be emitted optimally at a density of $n_{\rm e} = 4 \times 10^{15}$ cm^{-3}. This requires a density contrast of 4×10^5 for all three lines to be produced in the same region. The net blueshift of CVI Lyα with respect to the galaxy rest frame and P-Cygni profile may indicate outflow in the outer BLR.

In addition to their line cores, the He II λ4686 and C IV λ1549 lines in NGC 4051 have very broad blue wings with FWHM= 5400 km s^{-1} (Peterson et al. 2000). It is likely that the high velocity component is located closer to the central black hole than the low-velocity component. This is supported by the large RMS variability observed in broad He II (Peterson et al. 2000). The high velocity He II and C IV lines are then produced at high densities ($n_{\rm e} = 2 \times 10^{14} - 2 \times 10^{16}$ cm^{-3}), roughly 9×10^{-5} pc from the center (Fig. 10). Very broad O

VII is produced at a density of $n_e = 7 \times 10^{13}$ at 2×10^{-5} pc, four times closer to the central black hole. Broad (FWHM $\sim$ 5000 km s^{-1}), blue-shifted components of C IV and H-Lyα are common to a number of NLS1s (Rodriguez-Pascual et al. 1997), and have been attributed to an outflowing BLR (Leighly 2000).

With the structure of the line emitting regions shown in Fig. 10, we are led to ask why certain regions of parameter space are filled and others are not. The outer radius of the BLR may be set by the dust sublimation radius (Netzer & Laor 1993; Laor 2003), with $R_{sub} \simeq 0.2(L_{bol}/10^{46})^{1/2}$ pc. For NGC 4051, $R_{sub} \simeq 1.0 \times 10^{-2}$ pc, which is close to the estimated BLR outer radius in Fig. 10. The inner radius may be constrained to be greater than the ionizing UV emission region. For a disk blackbody emitting at 50% of the Eddington limit, $R_{BLR} > R_{UV} \sim 200R_G$ (5×10^{-6} pc). The lower right hand corner of Fig. 10 is empty, indicating that the highest density emission line regions have $n_e < 10^{17}$ cm^{-3}. The accretion disk density may set this upper limit for the BLR density, especially if it is the source of the BLR plasma. The lack of emission lines from the BLR with ionization greater than C VI may owe to insufficient S/N.

Observations are qualitatively consistent with a model where the BLR is formed as an accretion disk wind (Murray & Chiang 1997). In this scenario, gas from the disk is heated and rises to a location where it is exposed to and accelerated by UV photons. The velocity width of the broad lines is produced primarily by Keplerian rotation, but radial velocity shear in the wind yields a single-peaked profile. The broad base of the line comes from close in while the narrow core arises further from the black hole. An accelerating outflow would naturally span a large range of densities at any given radius, from the density of the neutral disk surface to the much lower density, highly ionized C VI emitting region observed with *XMM-Newton*. The BLR appears to span the entire range of allowed radii, from just outside the UV continuum emission region to where it merges (perhaps seamlessly) with the NLR. In the case of NLS1s such as NGC 4051, the distinction between the BLR and NLR may be artificial.

4.4. Narrow Line Region

The narrow N VI, O VII, Ne IX, and Si XIII emission lines require densities of $n_e = 10^7 - 10^8$ cm^{-3} at $r > 0.02$ pc (Fig. 10). These are below the critical densities of the forbidden lines ($\log n_{crit} \sim 9 - 13$) and consistent with the observed ($f/i > 3$) line ratios (Porquet & Dubau 2000). A low-state *Chandra* ACIS-S image of NGC 4051 shows little extended emission (Uttley et al. 2003b). This is different from other nearby Seyferts, including NGC 4151, Circinus, and NGC 1068 (Ogle et al. 2000; Sambruna et al. 2001;

Ogle et al. 2003) where the X-ray NLR is extended on the same size scale as the optical NLR.

The optical [O III] emission region has a smaller velocity width (FWHM = 240 km s^{-1}) than O VII (Fig. 10), and extends to a maximum distance of 220 pc from the nucleus (Christopoulou et al. 1997). (The contribution of the galactic stellar bulge to the virial mass dominates at these radii, leading to velocities of a couple hundred km s^{-1}.) The [O III] λ5007 line has a critical density of $n_e \sim 10^6$ cm^{-3}, which puts a lower limit of ~ 30 pc (0$''$7) on its inner emission radius. This implies that there may be a separation between the X-ray and optical narrow line regions.

The large fractional covering of the X-ray NLR by the ionized X-ray absorber requires the absorber to be at larger radius than the emitter ($r > 0.02$ pc). The conditions in the narrow absorber are likely to be similar to the emitter, but may have somewhat lower densities to attain the same ionization parameter at larger radius. If we assume they have the same density and radius, then the column densities in Table 1 give a radial thickness of $\sim 10^{13}$ cm, and radial filling factor of $\sim 10^{-4}$ for the ionized absorber-emitter. This small value, plus the large global covering fraction indicate a sheet-like morphology.

The accretion disk inclination implies a lower limit on the UV-X ionization cone opening half-angle of $\theta \geq 48°$. This is larger than the value of $\theta = 23°$ for the [O III] conical outflow model (Christopoulou et al. 1997). It appears that the [O III] cone is narrower than the full ionization cone. The O VII global covering fraction yields a half-opening angle of 77° for the X-ray ionization cone, which is larger than but consistent with the disk inclination angle. However, variability could cause us to overestimate the covering fraction and ionization cone opening angle.

We estimate the outflow rate of the O VII NLR, assuming it resides in a thin shell of covering fraction f_c. Combining the equation of continuity with the definition of the ionization parameter ξ, the mass outflow rate is

$$\dot{M}_{out} = 4\pi f_c \frac{L_{ion}}{\xi} \mu m_p v_r, \tag{1}$$

where $\mu = 1.3$ is the mean atomic weight per electron and $v_r = 400$ km s^{-1} is the observed radial outflow velocity of the absorber. Using $\log \xi = 1.0$ from our XSTAR simulation, $f_c = 0.76$ from the O VII f equivalent width, and $L_{ion} = 4.1 \times 10^{42}$ erg s^{-1}, we find a large mass outflow rate of $\sim 5 M_\odot$ yr^{-1}. This is a robust result since we have directly measured most of the variables in Equation 1. The quantity $f_c L_{ion}$ comes directly from the emission line normalization, averaged over the entire emission region. The absorber radial velocity is

probably a fair estimate of the mean flow velocity.

The estimated mass outflow rate is a factor of 10^3 greater than the nuclear accretion rate, assuming an efficiency of $\eta = 0.1$ (§4.1). The kinetic luminosity of the outflow is a significant fraction ($\sim 7\%$) of the ionizing luminosity of the AGN, but only a small fraction ($\sim 1\%$) of the bolometric luminosity. A lower (but still suprisingly large) mass outflow rate of $3 M_\odot$ yr^{-1} (10 times the accretion rate) is found for the O VII NLR of the broad-lined Seyfert 1 galaxy NGC 3783 (Behar et al. 2003). If AGN outflows are driven by radiation pressure, then there may be a connection between the near-Eddington luminosity of NGC 4051 and its large outflow rate. If this wind escapes the black hole, then the supply of fuel to the AGN will be exhausted more rapidly by outflow than by accretion.

A number of intrinsic UV absorption systems are observed by *HST*, with velocities ranging from $+30$ to -647 km s^{-1}, in ions Si II-IV, C II-IV, and N V (Collinge et al. 2001). The UV absorber components 1-4 are the closest in velocity (-647 to -337 km s^{-1}) to the X-ray absorbers we observe with *XMM-Newton*. The N V $\lambda 1239, 1243$ lines appear to be saturated and Collinge et al. (2001) do not give column density estimates for them. We predict a mean optical depth of the N V $\lambda 1239$ line of $\tau = 2.8$ from the N V column density (Table 1) and the UV line width of 730 km s^{-1}. Therefore we expect the UV lines to be nearly saturated, based on our X-ray observations. A similar result is found for NGC 5548 by Arav et al. (2003), who compare *XMM-Newton* and *FUSE* observations of O VI lines.

There is a strong trend in the ionized absorber-emitter of increasing column density with ionization parameter (Fig. 6). A linear least-squares fit to a power law $N_H = N_A \xi^\alpha$ (including only absorber N_H) gives an index of $\alpha = d \log N_H / d \log \xi = 0.5 \pm 0.2$ and intercept of $\log N_A = 20.0 \pm 0.3$. A similar trend is found in NGC 5548 by Steenbrugge et al (2003), with slope in the range 0.25 to 0.5. However, a power law gives a formally poor fit to the absorber column density distribution in NGC 4051. The distribution appears to peak at $\log \xi \sim 1.4$, with the column density dropping off at higher ionization parameter.

The ionization distribution of the absorber may either be continuous or consist of discrete phases. The 3.7 decades of ionization parameter observed in the NGC 4051 outflow (Fig. 6) require at least 2 phases. Two-phase models have been suggested as a way to confine photoionized clouds (Krongold et al. 2003, e.g.). More than one phase may exist at pressures where the heating curve is multi-valued (Krolik & Kriss 2001). We construct the heating curve for NGC 4051 (Fig. 12) using XSTAR and the SED (Fig. 2). We place absorber ions at their ionization parameters of peak abundance and find that not all ionization phases can be in pressure equilibrium. While there do exist segments of vertical slope and marginal stability on the curve, these only apply for the high ionization species N VII-Fe XX. The pressure of the lowest ionization phase of the absorber is as much as 100 times greater than

the pressure of the high ionization phases (Fig. 12).

It is a common property of Seyfert galaxies that the lower ionization UV and X-ray absorbers have lower column densities than their high ionization X-ray counterparts. While UV column density measurements are in some cases plagued by saturation and partial covering effects, this is less of a problem for the lower optical depth K-shell absorption lines in the X-ray spectrum (Arav et al. 2003). In the case of NGC 4051, the N VII absorber carries 100 times as much mass as the O IV absorber. This must be telling us something fundamental about how the NLR clouds are produced. Comparing Figs. 6 and 12, it appears that the highest column density ions, N VII-Fe XX, may reside in regions of marginal stability, perhaps confirming the prediction of Krolik & Kriss (2001). However, the lower ionization species must exist out of pressure equilibrium and may be rapidly destroyed by expansion and photoionization heating. This may potentially explain their lower column density. Gas pressure confinement is not necessary in a dynamic outflow which is continually replenished by the accretion disk.

5. Summary

XMM-Newton RGS observations of NGC 4051 demonstrate the capability of high-resolution X-ray spectroscopy to uncover the nature of AGN accretion and outflows at scales ranging from just outside the black hole event horizon to the narrow line region. The soft X-ray excess emission is a combination of continuum and relativistic emission line components. It is incorrect to fit this with simple models such as a power law or blackbody. It is important to get the continuum model correct for fitting the spectra of ionized absorbers. Conversely, it is essential to account for ionized absorption in order to accurately measure the underlying continuum and relativistic emission lines.

5.1. Relativistic Emission Lines

We successfully model the soft X-ray excess in the spectrum of NGC 4051 as a power law plus relativistic O VIII emission, including Lyα, higher-order emission lines, and recombination continuum. The line profiles require emission from inside the last stable orbit of a Schwarzschild black hole, or emission close to the last stable orbit of a Kerr black hole. The relativistic emission line region has an inner radius of $< 1.7R_{\mathrm{G}}$, which may indicate a rapidly spinning black hole. The accretion disk is viewed at a relatively high inclination of $48°$. Together with the reverberation mass of $5 \times 10^5 M_{\odot}$, this confirms that NGC 4051

contains a relatively low-mass black hole.

The spectrum of NGC 4051 is quite different from those of MCG-6-30-15 and Mrk 766. The relativistic O VIII line in NGC 4051 is considerably broader, and there is no indication of relativistic N VII or C VI emission lines. The lack of relativistic C VI and N VII emission is consistent with solar abundances and a high ionization parameter ($\log \xi > 3.4$). This contrasts with MCG-6-30-15 and Mrk 766, which require super-solar abundances or resonance fluorescence effects to explain strong N VII emission. Photoionization modeling indicates that the relativistic line emission comes from the thin, high density ($n \sim 10^{17}$ cm^{-3}) photoionized skin of the accretion disk. The ~ 90 eV equivalent width of O VIII Lyα can consistently be produced in the this layer, with an additional contribution from higher order Lyman transitions.

5.2. Ionized Absorber-Emitter

We fit an ionized absorber-emitter model for several ions in the narrow-line spectrum of NGC 4051. The ions cover nearly 4 decades of ionization parameter. The column density increases with ionization parameter, with high ionization states carrying more mass than lower ionization states. The absorber and emitter have similar ionic column densities, and the X-ray NLR is covered by the absorber, indicating that the two arise in the same region. The large global covering fraction and high velocity of the X-ray NLR imply a mass outflow rate which is 10^3 times greater than the accretion rate. An analysis of the heating curve in the photoionized absorber shows that the low ionization UV-X absorber can not be in pressure equilibrium with the higher ionization phases of the X-ray absorber.

We find evidence for Doppler-broadened C VI and O VII emission lines in the X-ray spectrum. The C VI emission line has a velocity width of 1200 km s^{-1}, similar to the UV and optical broad lines. This may indicate a high ionization component within the BLR of NGC 4051. The implied large range of densities and observed P-Cygni line profiles are consistent with the BLR arising in an accretion disk wind. A very broad (FWHM $\sim 11,000$ km s^{-1}) O VII line may arise in the innermost regions of the BLR, just exterior to the UV emitting portion of the accretion disk.

5.3. Low-state Spectrum

Observation of NGC 4051 during a low X-ray flux state shows high equivalent width narrow emission lines. The X-ray NLR does not respond to rapid X-ray continuum variations,

consistent with its estimated 0.02 pc size scale. However, we find evidence for low ionization Fe UTA absorption during the low-state, which is not present during the high state. The source is too weak during the low state to measure the relativistic O VIII feature.

REFERENCES

Agol, E., & Krolik, J. H. 2000, ApJ, 528, 161

Anders, E., & Grevesse, N. 1989, Geochimica et Cosmochimica Acta, 53, 197

Arav, N., Kaastra, J., Steenbrugge, K., Brinkman, B., Edelson, R., Korista, K. T., & de Kool, M. 2003, ApJ, 590, 174

Ballantyne, D. R., Iwasawa, K. & Fabian, A. C. 2001, MNRAS, 323, 506

Ballantyne, D. R., Ross, R. R., & Fabian A. C., 2002, MNRAS, 336, 867

Ballantyne, D. R., Vaughan, S., & Fabian A. C., 2003, MNRAS, 342, 239

Behar, E. et al. 2003, ApJ, 598, 232

Behar, E. & Netzer, H. 2002, ApJ, 570, 165

Boller, Th., Brandt, W. N., & Fink, H. 1996, A&A, 305, 53

Boller, Th., Tanaka, Y., Fabian, A., Brandt, W. N., Gallo, L., Anabuki, N., Haba, Y., & Vaughan, S. 2003, MNRAS, L343, 89

Brookings, T., & Ogle, P. M. 2003 *IMP–IDL Multi-Purpose Fitting User Guide*

Branduardi-Raymont, G., Sako, M., Kahn, S., Brinkman, A. C., Kaastra, J. S., & Page, M. J. 2001, A&A, L140

Cash, 1979, ApJ, 228, 939

Christopoulou, P. E., Holloway, A. J., Steffen, W., Mundell, C. G., Thean, A. H. C., Goudis, C. D., Meaburn, J., & Pedlar, A. 1997, MNRAS, 284, 385

Collinge, M. J., et al. 2001, ApJ, 557, 2

den Herder, J. W., et al. 2001, A&A, 365, L7

Dickey, J. M. & Lockman, F. J. 1990, ARAA, 28, 215

Fabian, A. C., Rees, M. J., Stella, L., & White, N. E., MNRAS, 238, 729

Fabian, A. C., Nandra, K., Reynolds, C. S., Brandt, W. N., Otani, C., & Tanaka, Y. 1995, MNRAS 277, L11

Gehrels, N. 1986, ApJ, 303, 336

Goodrich, R. W. 1989, ApJ, 342, 224

Guainazzi, M., Mihara, T., Otani, C., & Matsuoka, M. 1996, PASJ, 48, 781

Gu, M. F., 2002, *FAC 0.8.8 Manual*

Kaastra, J. S., Steenbrugge, K. C., Raassen, A. J. J., van der Meer, R. L. J., Brinkman, A. C., Liedahl, D. A., Behar, E., & de Rosa, A. 2002, A&A, 386, 427

Kallman, T. R., & McCray, R., 1982, ApJS, 50, 263

Kallman, T. R. 2002, *XSTAR, A Spectral Analysis Tool, V2.1*

Kirsch, M., et al. 2003, Document XMM-SOC-CAL-TN-0018, ESA

Krolik, J. H., & Kriss, G. A. 2001, ApJ, 561, 684

Krolik, J. H. 2001, ApJ, 551, 72

Krongold, Y., Nicastro, F., Brickhouse, N. S., Elvis, M., Liedahl, D. A., & Mathur, S., 2003, ApJ, 597, 832

Laor, A. 1991, ApJ, 376, 90

Laor, A. 2003, ApJ, L590, 86

Lee, J.C., Ogle, P.M., Canizares, C. R., Marshall, H. L., Schulz, N. S., Morales, R., Fabian, A. C., & Iwasawa, K. 2001, ApJ, 554, L13

Leighly, K. M. 2000, NewAR, 44, 395

Leighly, K. M. 1999, ApJS, 125, 297

McHardy, I. M., Green, A. R., Done, D., Puchnarewicz, E. M., Mason, K.O., Branduardi-Raymont, G., & Jones, M. H. 1995, MNRAS, 273, 549

McKernan, B., Yaqoob, T., George, I. M., & Turner, T. J. 2003, ApJ, 593, 142

Mason, K. O., et al. 2002, ApJ, L580, 117

Mason, K. O., et al. 2003, ApJ, 582, 95

Murray, N., & Chiang, J. 1997, ApJ, 474, 91

Nandra, K., George, I. M., Mushotzky, R. F., Turner, T. J., & Yaqoob, T. 1997a, ApJ, 476, 70

Nandra, K., George, I. M., Mushotzky, R. F., Turner, T. J., & Yaqoob, T. 1997b, ApJ, 477, 602

Nayakshin, S., Kazanas, D., & Kallman, T. R. 2000, ApJ, 537, 833

Netzer, H., & Laor, A., 1993, ApJ, 404, L51

Novikov, I. D., & Thorne, K. S. 1973. in *Black Holes*, ed. C. DeWitt & B. DeWitt, (New York: Gordon and Breach).

Nowak , M. A., & Chiang, J. 2000, ApJ, 531, L13

Ogle, P. M., Marshall, H. L., Lee, J. C., & Canizares, C. R. 2000, ApJ, L81

Ogle, P. M., Brookings, T., Canizares, C. R., Lee, J. C., & Marshall, H. L. 2003, A&A, 402, 849

Ogle, P. M., & Brookings, T. 2003 *IMP–IDL Multi-Purpose Fitting Spectroscopy Guide*

Page, M. J., Mason, K. O., Uttley, P., McHardy, I. M., & Ogle, P. M., MNRAS, in prep.

Page, M. J., et al. 2001, A&A, 365, 152

Peterson, B. M. et al. 2000, ApJ, 542, 161

Pounds, K. A., Reeves, J. N., Page, K. L., Wynn, G. A., & O'Brien, P. T. 2003, MNRAS, 342, 1147

Porquet, D., & Dubau, J. 2000, A&AS, 143, 495

Reynolds, C. S., Ward, M. J., Fabian, A. C., & Celotti, A. 1997a, MNRAS, 291, 403

Reynolds, C. S., & Begelman, M. C. 1997b, ApJ, 488, 109

Rodriguez-Pascual, P. M., Mas-Hesse, J. M., & Santos-Lleo, M. 1997, A&A, 327, 72

Sako, M., et al. 2003a, ApJ, 596, 114

Sako, M. 2003b, ApJ, 594, 1108

Salvi, N. J, et al. 2003a, MNRAS, in press

Salvi, N. J., Mason, K. O., Ogle, P. M. et al. 2003b, MNRAS, in prep.

Salvi, N. J. 2003, PhD Thesis, University of London

Sambruna, R. M., Netzer, H., Kaspi, S., Brandt, W. N., Chartas, G., Garmire, G. P., Nousek, J. A., & Weaver, K. A. 2001, ApJ, 546, L13

Shakura, N. I., & Sunyaev, R. A. 1973, A&A, 24, 337

Shemmer, O., Uttley, P., Netzer, H., & McHardy, I. M. 2003, MNRAS, 343, 1341

Socrates, A., Davis, S. W., & Blaes, O. 2003, ApJ, in press (astro-ph/0307158)

Steenbrugge, K. C., Kaastra, J. S., de Vries, C. P., & Edelson, R. 2003, A&A, 402, 477

Tanaka, Y., et al. 1995, Nature, 375, 659

Titarchuk, L., 1994, ApJ, 434, 570

Turner, T. J., et al. 2001, ApJ , 548, L13

Uttley, P. Taylor, R. D., McHardy, I. M., Page, M. J., Mason, K. O., Lamer, G., & Fruscione, A. 2003, MNRAS, in press (astro-ph/0310701)

Uttley, P., Fruscione, A., McHardy, I., & Lamer, G. 2003, ApJ, 595, 656

Vaughan, S., Pounds, K. A., Reeves, J. Warwick, R., & Edelson, R. 1999, MNRAS, 308, L34

Verheijen, M. A. W., & Sancisi, R. 2001, A&A 370, 765

Verner, D. A., Verner, E. M., & Ferland, G. I 1996a, Atomic Data Nucl. Data Tables, 64, 1

Verner, D. A., Ferland, G. J., & Yakovlev, D. G., 1996b, ApJ, 465, 487

Wilms, J., Reynolds, C. S., Begelman, M. C., Reeves, J., Molendi, S., Stuabert, R., & Kendziorra, E. 2001, MNRAS, 328, L27

Table 1.   High state absorber and emitter column densities

Ion	$N_{\mathrm abs}$[a]	$N_{\mathrm em}$[b]	$N_{\mathrm H,abs}$[c]
C V	5^{+1}_{-1}	$\cdots$	2
C VI	33^{+3}_{-2}	22^{+3}_{-2}	16
N II	$0.6^{+0.4}_{-0.3}$	$\cdots$	0.7
N III	<0.2	$\cdots$	<0.3
N IV	$0.2^{+0.2}_{-0.1}$	$\cdots$	0.3
N V	$0.5^{+0.2}_{-0.2}$	$\cdots$	1
N VI	$2.5^{+0.7}_{-0.6}$	$1.9^{+0.8}_{-0.7}$	3.1
N VII	19^{+4}_{-3}	9^{+4}_{-3}	31
O IV	$1.3^{+0.7}_{-0.6}$	$\cdots$	0.26
O V	$2.0^{+0.9}_{-0.7}$	$\cdots$	0.56
O VI	$1.7^{+0.8}_{-0.6}$	$\cdots$	0.53
O VII	30^{+3}_{-3}	23^{+3}_{-3}	5.0
O VIII	38^{+10}_{-4}	27^{+9}_{-8}	8.5
Ne IX	6^{+4}_{-3}	13^{+4}_{-4}	7
Fe I	<0.2	$\cdots$	<2
Fe XVII	$2.1^{+0.6}_{-0.5}$	$0.8^{+0.4}_{-0.3}$	13
Fe XVIII	$1.0^{+0.3}_{-0.2}$	$0.4^{+0.2}_{-0.2}$	6.3
Fe XIX	$1.2^{+0.3}_{-0.2}$	$1.9^{+0.5}_{-0.5}$	7.4
Fe XX	$2.2^{+0.3}_{-0.2}$	5^{+1}_{-1}	14

[a]Absorber ionic column density $(10^{16}\ \mathrm{cm}^{-2})$

[b]Emitter ionic column density $(10^{16}\ \mathrm{cm}^{-2})$

[c]Equivalent absorber hydrogen column density $(10^{20}\ \mathrm{cm}^{-2})$, assuming solar elemental abundances (Anders & Grevesse 1989).
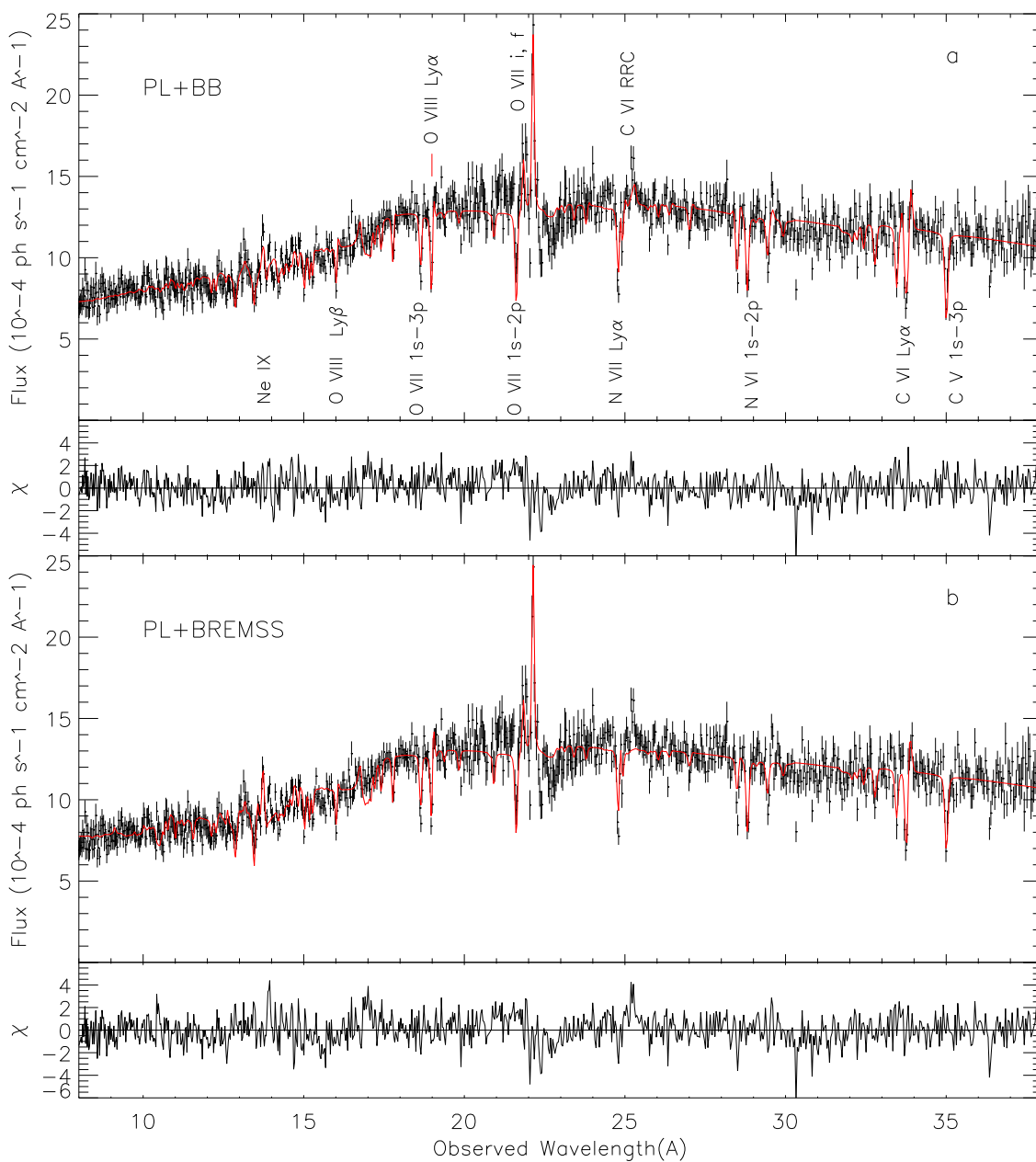
Fig. 1.— Continuum model fits to the *XMM-Newton* RGS spectrum of NGC 4051. Narrow absorption and emission lines are also included for various ions of C, N, O, Ne, and Fe. a) Power law plus single blackbody. b) Power law plus bremsstrahlung. These are both poor fits, and fail to match the observed soft excess without overestimating the O VII edge depth.
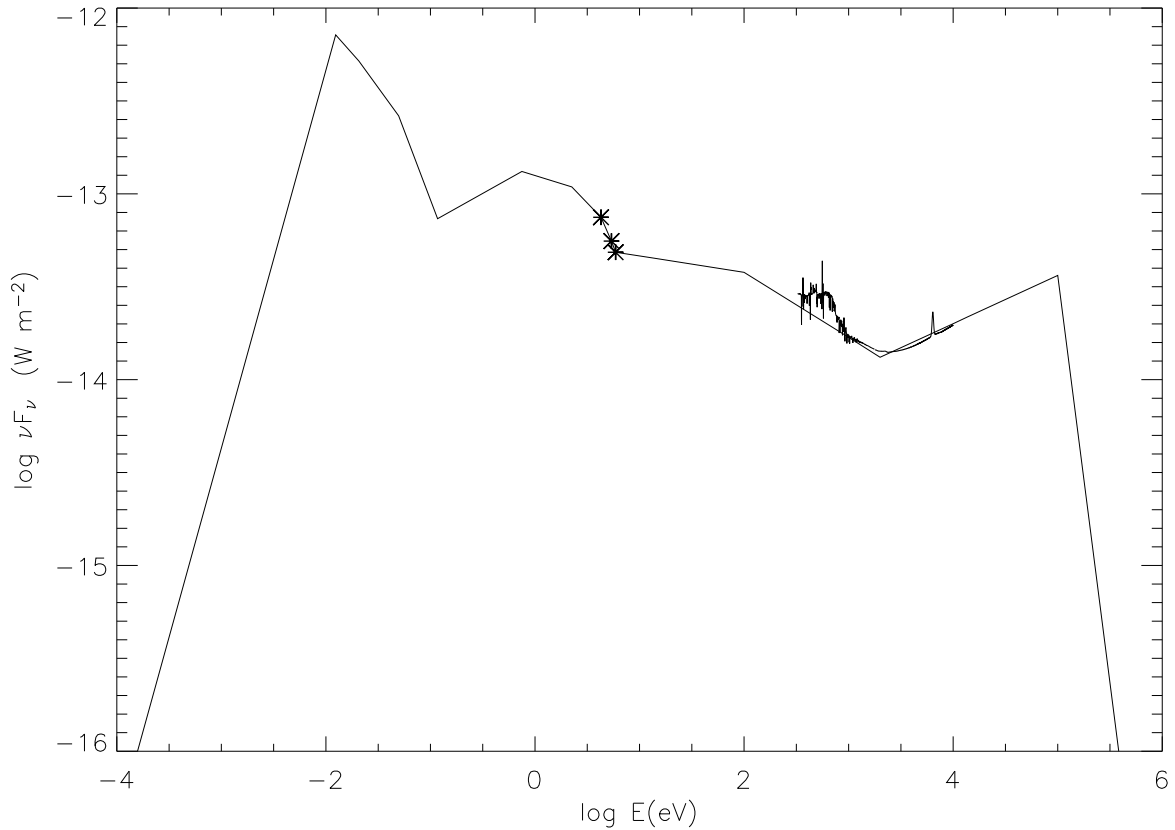
Fig. 2.— NGC 4051 high-state spectral energy distribution. Best-fit RGS and EPIC models (corrected for Galactic absorption) are over-plotted. *XMM-Newton* OM UV fluxes, corrected for Galactic reddening, are indicated with asterisks. Additional radio-optical data points are from NED, and we choose a hard X-ray cut-off at 100 keV. The soft X-ray bump at 0.3-1 keV emits a small fraction of the total AGN luminosity, and is unlikely to be black body emission from the accretion disk. Most of the luminosity from the accretion disk is radiated in the optical-UV big blue bump.
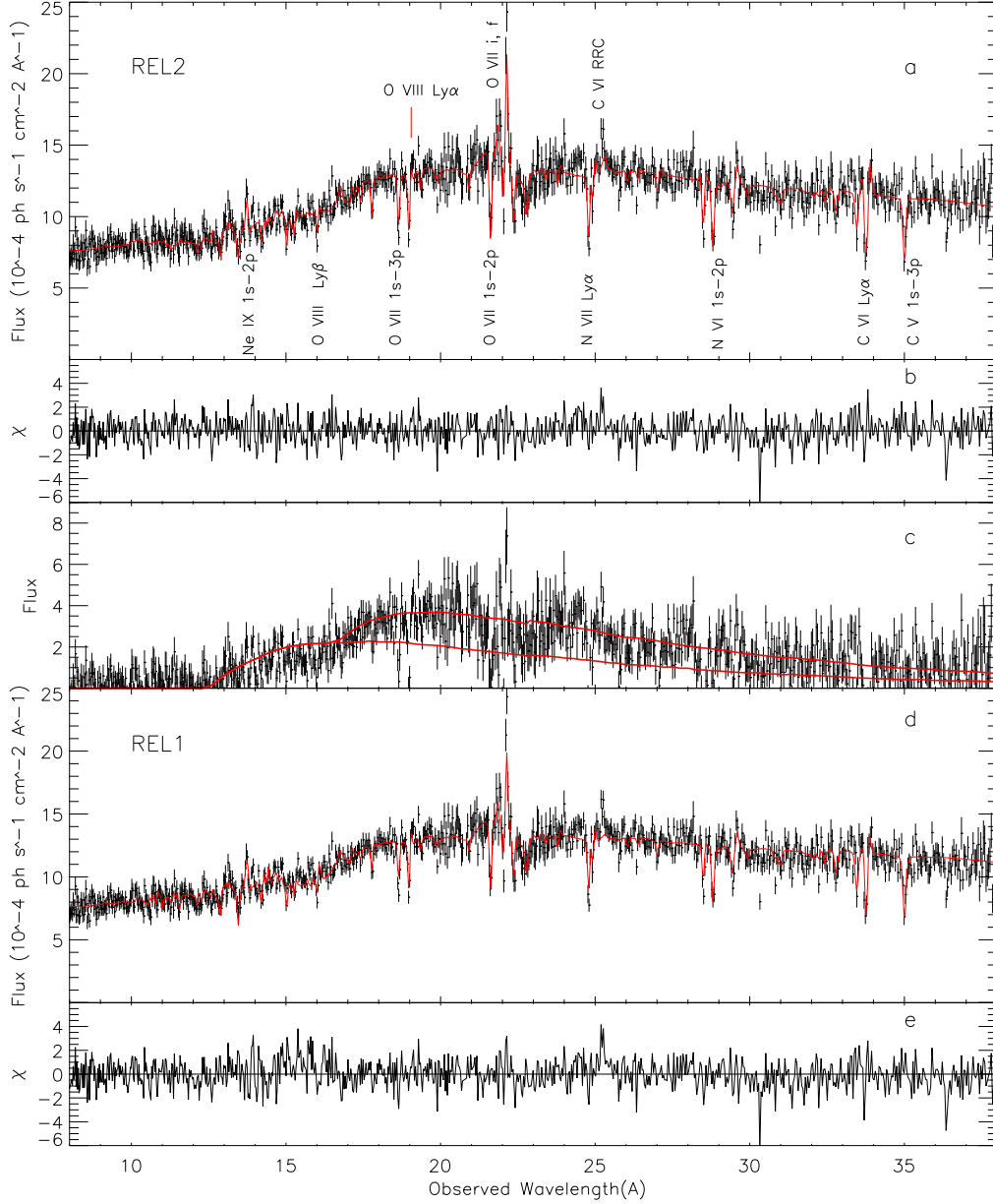
Fig. 3.— a) Complete relativistic O VIII series (REL2) and d) Ly α-only (REL1) model fits to the *XMM-Newton* RGS spectrum of NGC 4051. Both models contain an underlying steep power law continuum ($\Gamma \sim 2.4$). Narrow absorption and emission lines are also included for various ions of C, N, O, Ne, and Fe. REL2 improves upon REL1 by adding in the O VIII Lyβ and higher-order relativistic emission lines and RRC. The middle panel (c) shows the residual O VIII emission after subtracting away the absorbed power-law continuum and narrow emission lines. A large fraction of the relativistic O VIII flux is from high order lines.
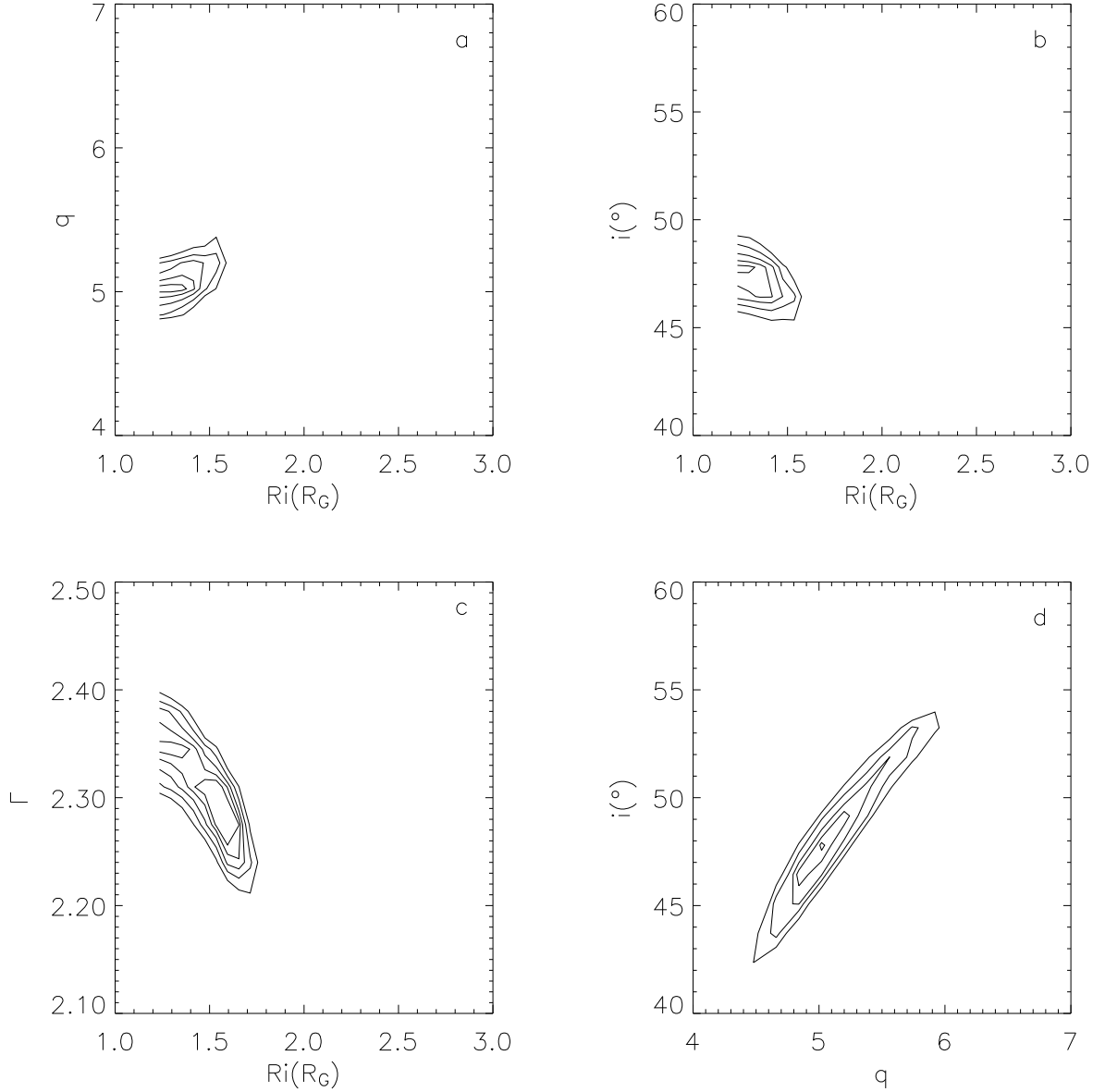
Fig. 4.— Confidence contours $(1 - 5\sigma)$ for relativistic emission line (REL2) fit. a-c) The inner radius $R_i < 1.7 R_G$ is well constrained by the RGS data. a) Radial emissivity index vs. R_i. b) Inclination vs. R_i. c) Power law continuum photon index vs. R_i, showing dependence of disk inner radius on model continuum shape. d) There is some degeneracy between disk inclination angle i and emissivity index q, but they are still well constrained by the REL2 model.
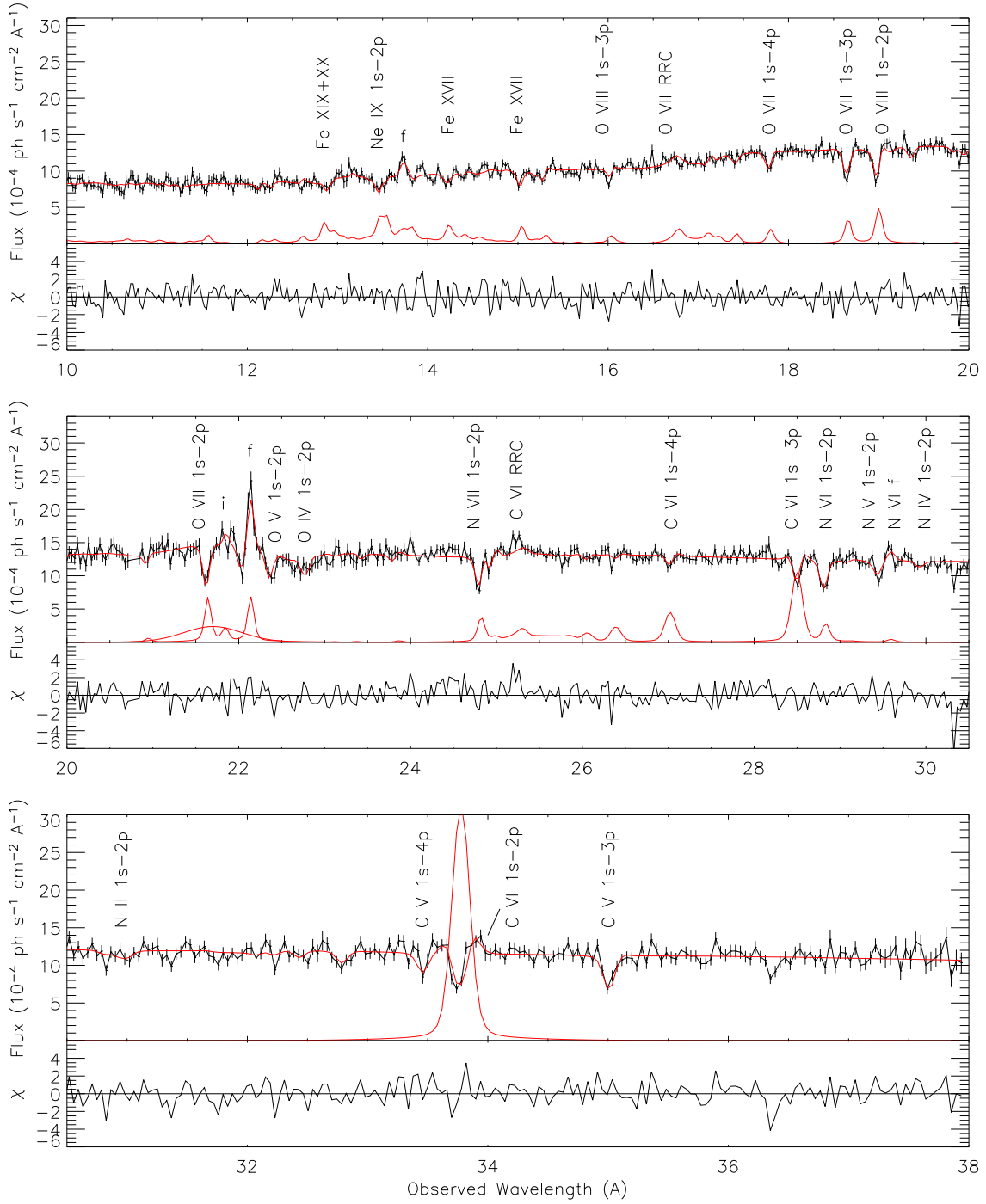
Fig. 5.— High-state RGS spectrum of ionized absorber-emitter (REL2 model).
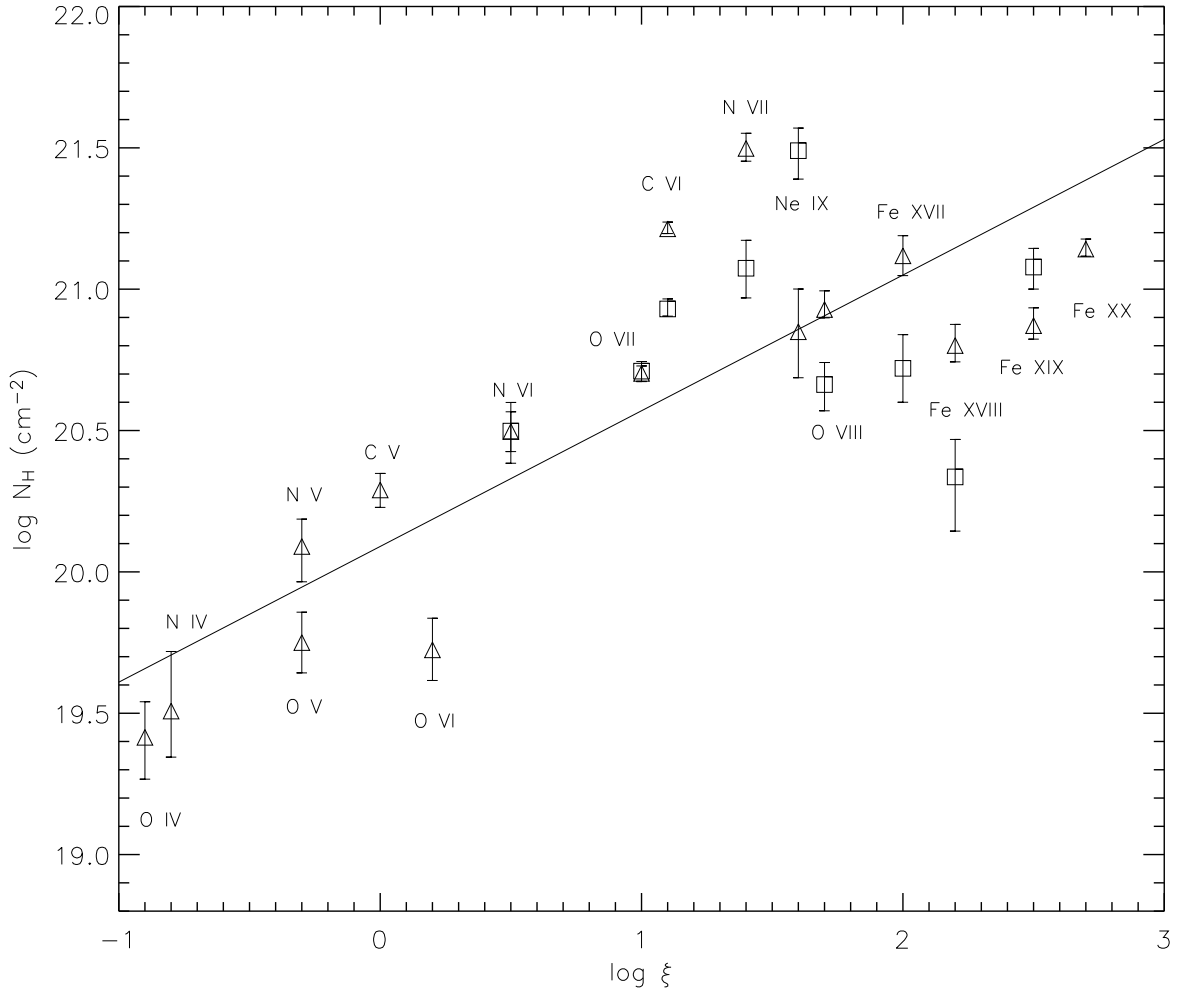
Fig. 6.— Ionized absorber-emitter column density distribution. Equivalent hydrogen column densities N_H for absorber (triangles) and emitter (squares) are plotted vs. ionization parameter ξ. There is an overall trend of increasing column density with ionization parameter. A power law fit is indicated by the solid line. The observed distribution appears to peak at $\log \xi \sim 1.4$.
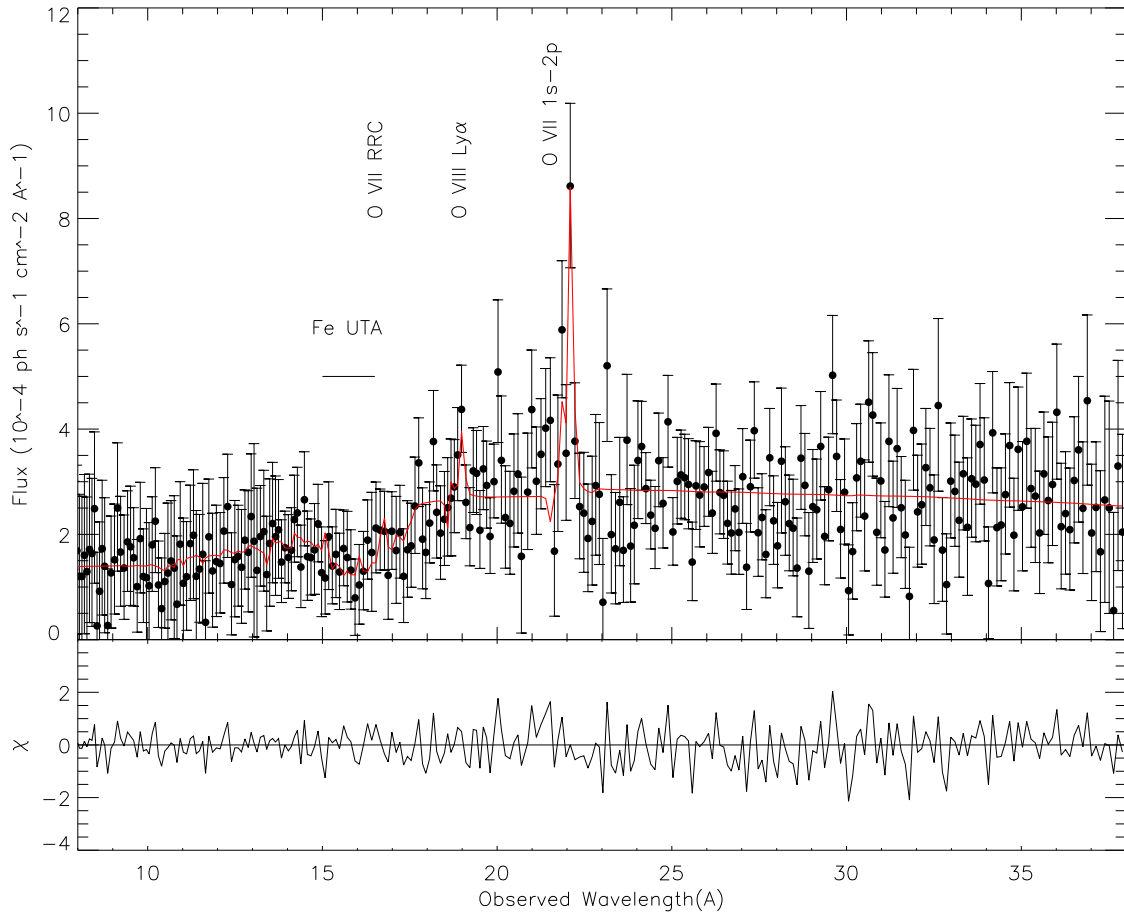
Fig. 7.— Model fit to the *XMM-Newton* RGS low-state spectrum of NGC 4051. The continuum is well described by a power law with $\Gamma = 2.6$. Adding relativistic O VIII emission does not improve the fit. Note the large EW O VII narrow line and possible Fe UTA.
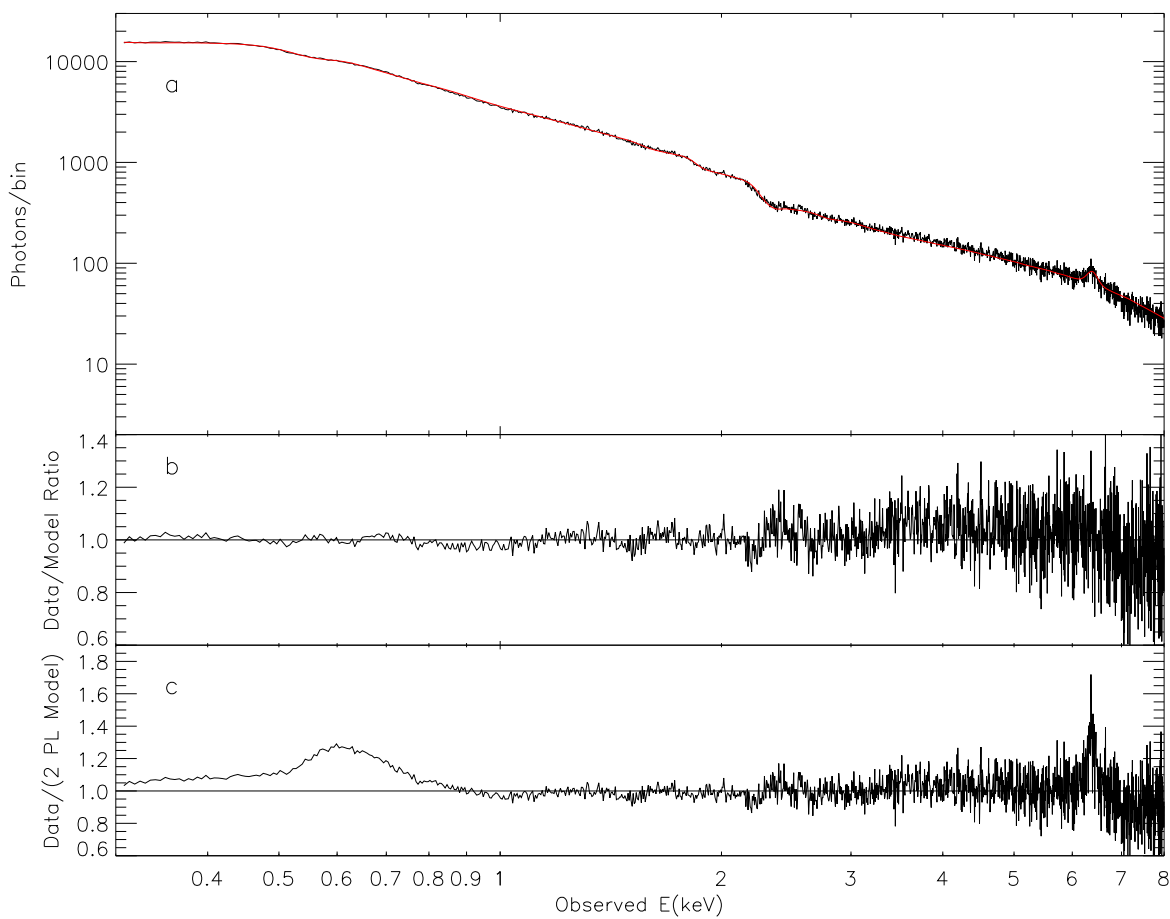
Fig. 8.— a) EPIC PN spectrum and model. The model consists of hard and soft power-law continua plus relativistic O VIII and Fe XXV emission lines. Narrow O VII and Fe Kα emission lines are also included. b) Ratio of data to model. c) Ratio of data to hard plus soft power law continua with Galactic absorption. The large bump at 0.6 keV is a combination of relativistic O VIII and narrow O VII emission lines. The narrow line at 6.3 keV is low-ionization Fe Kα.
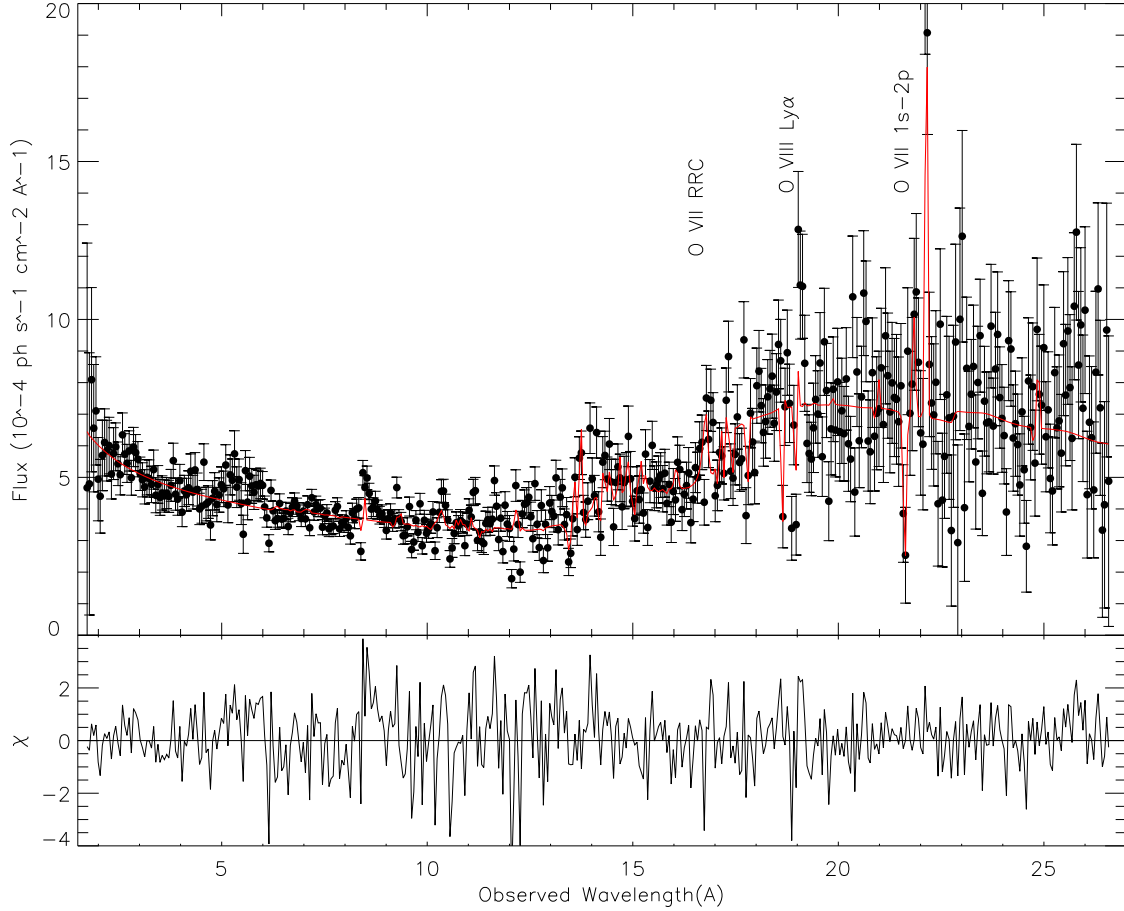
Fig. 9.— *Chandra* HETG (MEG) spectrum of NGC 4051. The underlying continuum is fit by hard plus soft power laws, and the broad bump in the soft excess is fit by relativistically broadened O VIII emission. Note the secondary excess at 13-17 Å, corresponding to blended high-order relativistic emission lines. Emission and absorption from the ionized outflow are also included in the model.
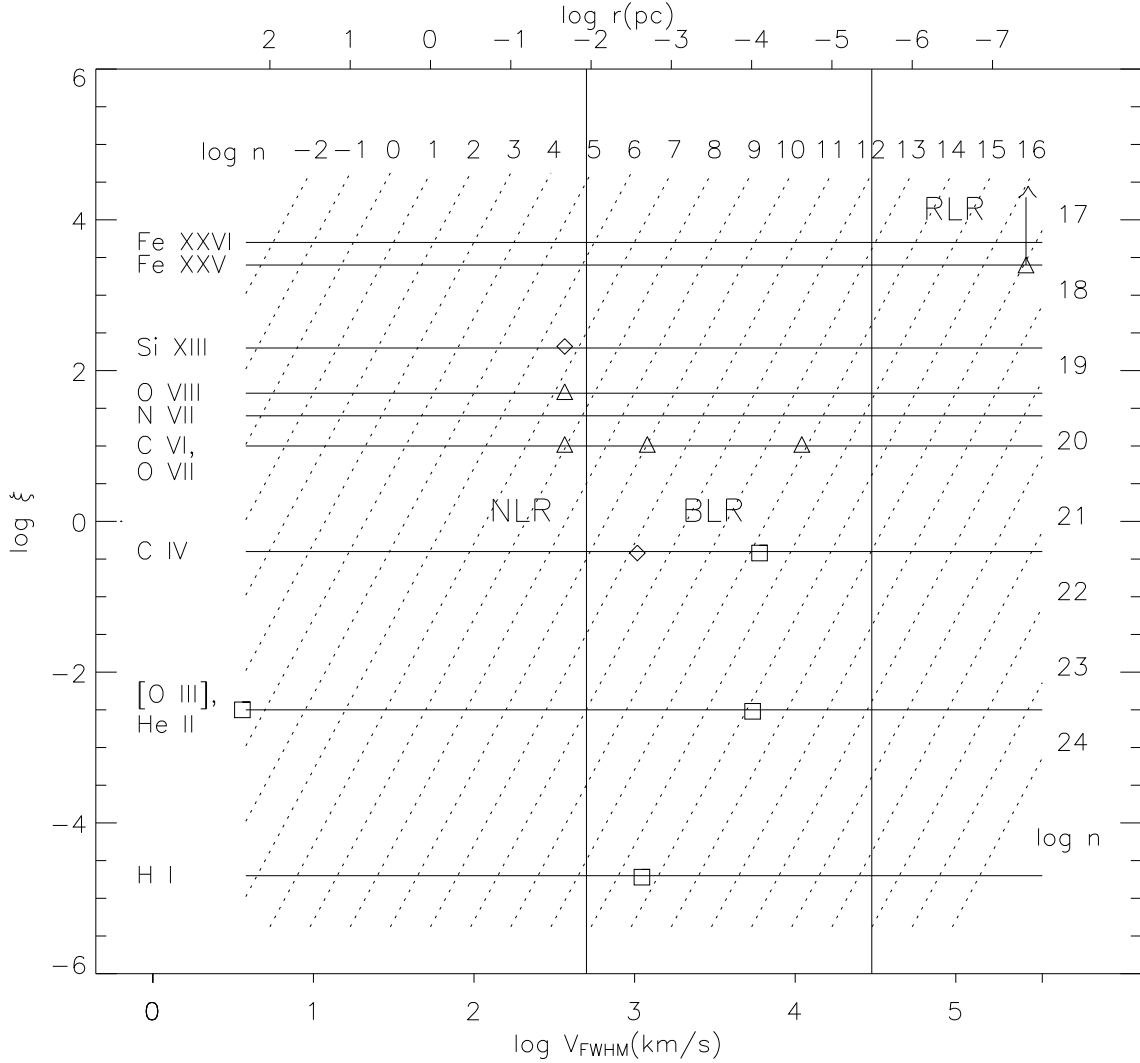
Fig. 10.— Ionization map of NGC 4051 NLR, BLR, and RLR. Dotted diagonal lines give ionization parameter ξ vs. Keplerian velocity for densities in the range $\log n(\mathrm{cm}^{-3}) = -2$ to 24 and $\log L_{\mathrm{ion}}(\mathrm{erg\ s}^{-1}) = 42.6$. Velocity, from measured line FWHM, is converted to radial distance assuming isotropic circular orbits around a $5 \times 10^5 M_\odot$ black hole. The exceptions are narrow [O III] and relativistic O VIII velocities computed from emitter radii. Vertical lines split the emission line regions by velocity into NLR, BLR, and RLR. Horizontal lines give ionization parameter of peak emissivity for prominent emission lines. Data are plotted as triangles (*XMM-Newton*, this work), diamonds (Collinge et al. 2001), and squares (Peterson et al. 2000).
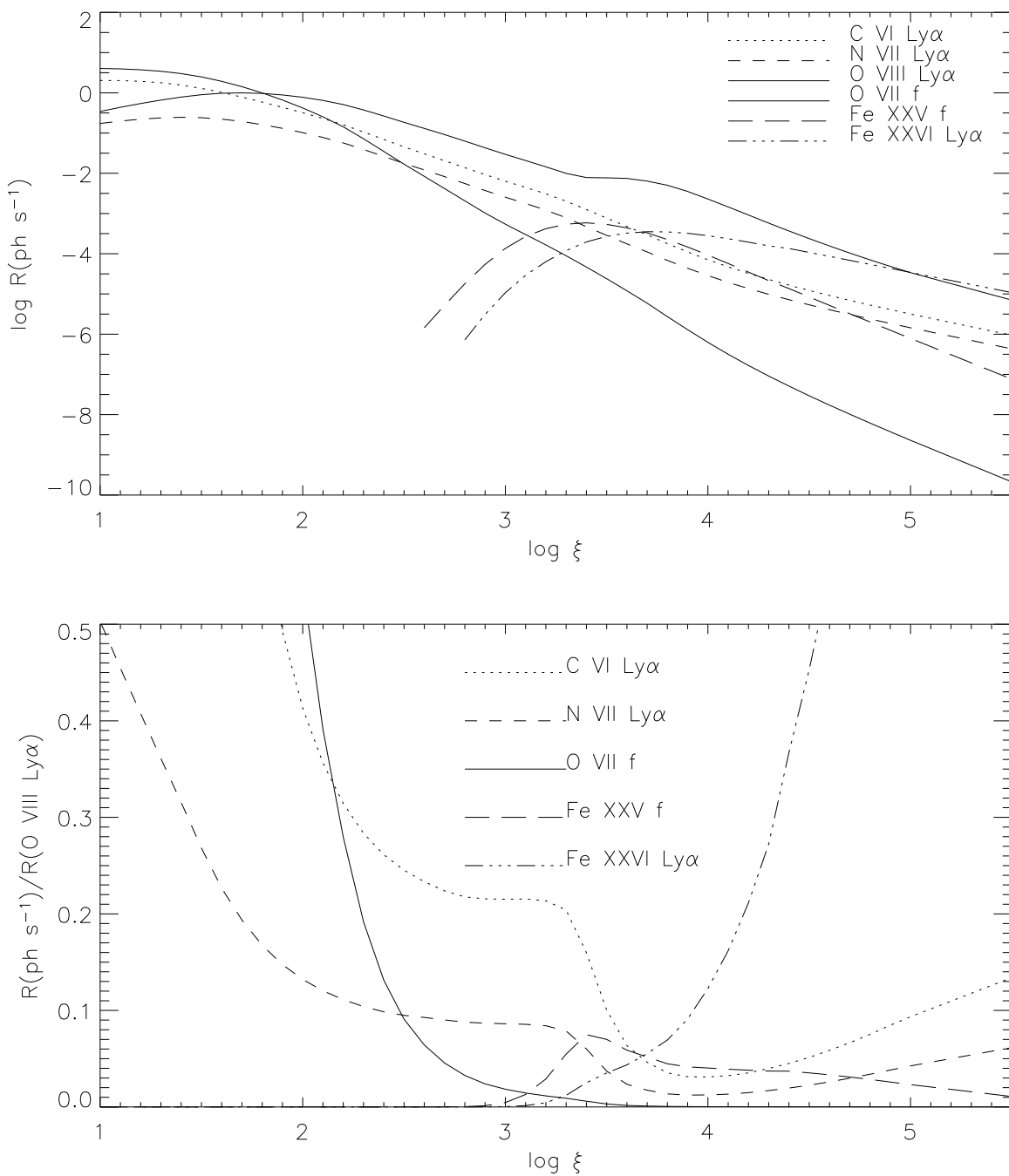
Fig. 11.— Emission lines from an optically thin photoionized plasma with solar abundances. a) Selected H-like and He-like $n = 2 - 1$ line strengths are plotted as a function of ionization parameter. b) Ratio of line strengths to O VIII Lyα. The RLR must be located at $\log \xi > 3.4$ to explain the lack of C VI emission. Fe XXV and XXVI are the dominant Fe charge states at this ionization parameter.
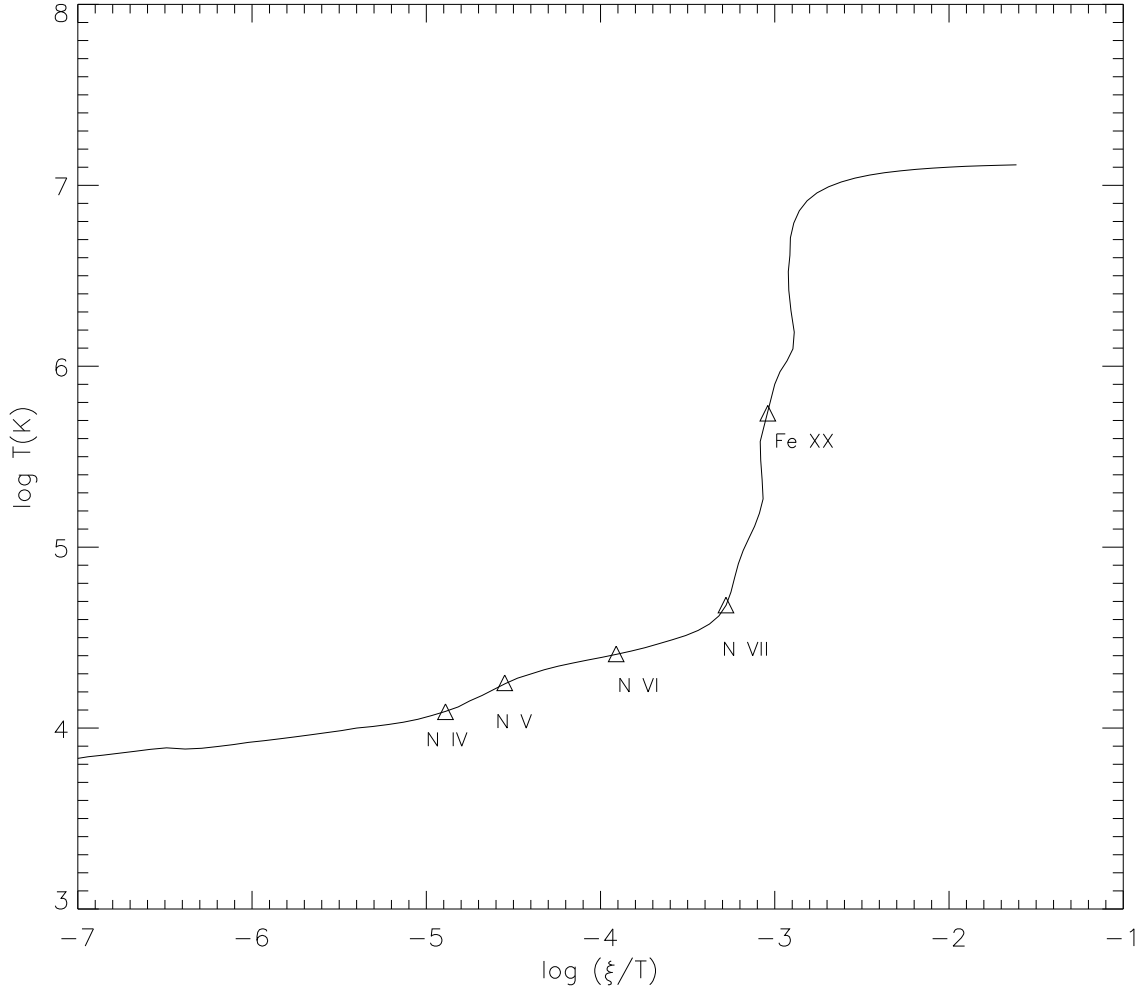
Fig. 12.— Thermal equilibrium (heating) curve for photoionized plasma, computed with XSTAR and NGC 4051 SED (Fig. 2). N IV-VII and Fe XX absorbers are indicated, assuming peak ionic abundances. The ordinate $\xi/T \sim F_{\rm ion}/P$ is inversely proportional to the gas pressure, which *decreases* to the right. If all ions are located at the same radius, the ionizing flux $F_{\rm ion}$ is constant. The observed ionization states cover a factor of 100 in pressure, and are *not* all in pressure equilibrium.